Pacific Northwest
NATIONAL LABORATORY

PNNL-36836

# Nondestructive Evaluation of Electron Beam Welds

June 2024

Richard E. Jacob
Nicholas Conway
Chris A. Hutchinson
Erin Kinney
Matthew S. Prowant

Prepared for the U.S. Nuclear Regulatory Commission
Office of Nuclear Regulatory Research
Under Contract DE-AC05-76RL01830
Interagency Agreement: NRC-31310022S022

PACIFIC NORTHWEST NATIONAL LABORATORY
*operated by*
BATTELLE
*for the*
UNITED STATES DEPARTMENT OF ENERGY
*under Contract DE-AC05-76RL01830*

**Printed in the United States of America**

**Available to DOE and DOE contractors from**
**the Office of Scientific and Technical Information,**
**P.O. Box 62, Oak Ridge, TN 37831-0062**
**www.osti.gov**
**ph: (865) 576-8401**
**fax: (865) 576-5728**
**email: reports@osti.gov**

**Available to the public from the National Technical Information Service**
**5301 Shawnee Rd., Alexandria, VA 22312**
**ph: (800) 553-NTIS (6847)**
**or (703) 605-6000**
**email: info@ntis.gov**
**Online ordering: http://www.ntis.gov**

PNNL-36836

# Nondestructive Evaluation of Electron Beam Welds

June 2024

Richard E. Jacob
Nicholas Conway
Chris A. Hutchinson
Erin Kinney
Matthew S. Prowant

Prepared for the U.S. Nuclear Regulatory Commission
Office of Nuclear Regulatory Research
Under Contract DE-AC05-76RL01830
Interagency Agreement: 31310022S0022

Carol A. Nove—NRC Contracting Officer Representative

Pacific Northwest National Laboratory
Richland, Washington 99354

# Summary

Pacific Northwest National Laboratory performed confirmatory nondestructive evaluation (NDE) research for the U.S. Nuclear Regulatory Commission (NRC) on mockups fabricated using electron beam welding (EBW). A key step in the acceptance of advanced manufacturing technologies in commercial nuclear power plants will be the assurance that components meet requirements established for inservice inspection. The purpose of the work was to study the inspectability of the EBW mockups using NDE techniques. Four blocks were constructed with simple square butt welds; these types of welds are characterized by vertical, machined surfaces joined with a through-wall weld with no filler material. Block 1 was welded with ideal parameters, block 2 had a small lack of fusion (LOF) defect and a through-wall keyhole defect, block 3 had a large LOF defect, and block 4 had a shallow lack of penetration (LOP) defect along the entire length of the weld joint. All blocks were carbon steel and were 90 mm thick on one side of the weld and 100 mm on the other. In addition to radiography, three different ultrasonic testing (UT) methods were tested: time of flight diffraction (TOFD), full matrix capture (FMC), and tandem pitch-catch.

The TOFD ultrasonic approach (a pitch-catch arrangement with probes facing each other across the weld) was superior to the other ultrasonic methods for both detection and sizing. All the defects, including the LOP in block 4, were readily detected. The results of this work suggest using the TOFD approach when dual-sided access is available for examining the types of EBW joints described in this report. For two reasons, we suggest that additional training will be needed to familiarize inspectors with how to recognize and interpret the types of signal responses when using this TOFD method. First, the defect signatures in the TOFD signals were different from those of conventional pulse-echo (PE) UT. The TOFD flaw responses were characterized by weak signals because the sound was blocked by the unfused joints, whereas conventional PE flaw responses are characterized by strong signals that are echoes back to the probe. Second, the defect signatures in the TOFD signals were different from those of conventional TOFD, in which tip-diffracted signals are of primary interest. The TOFD approach used in this report did not use tip-diffracted signals.

The FMC ultrasonic approach using a single probe in a PE setup showed corner echoes from LOF sections in plates 2 and 3, the keyhole defect in plate 2, and the fusion line in plate 3. The LOP defect in plate 4 was faintly visible in the side view. Otherwise, defect depth information was not readily seen. Indeed, we observed that the signals from a fused region and an unfused region looked the same. The FMC images also showed some weak signals from the weld region, likely due to scatter from the altered microstructure. The smooth, vertical, planar joint line geometry of these blocks differs from the fusion lines seen in most conventional V welds, where the fusion planes are angled. Thus, the EBW joint line geometry poses particular challenges to standard PE inspection techniques, including FMC, because the echoes are reflected away from the probe.

A tandem ultrasonic approach (a pitch-catch arrangement with probes arranged one behind the other on the same side of the weld) detected strong corner echoes in blocks 2 and 3 along the unfused lengths; however, it did not provide any information about the depth of the LOF defects. Signals indicative of weld root were observed in the blocks, but there was no indication of the LOP defect in block 4. We speculate that a dynamic tandem approach, in which the probe spacing is varied, would provide better results, but the complexity of executing such a method will require additional development. The dynamic tandem approach would be particularly useful when access is restricted to a single side of the weld.

We did not find the radiography to be helpful in identifying the nature of the defects beyond what was apparent from visual observation. The weld joints were too narrow to provide sufficient x-ray contrast. The thickness of the blocks was another limiting factor; the x-ray settings required to penetrate the blocks resulted in significant backscatter that compromised image quality. Even if defects could be identified with radiography, it is unlikely that any depth information could be obtained.

In addition to describing the empirical work, this report summarizes the findings of a 2023 NRC-hosted public workshop on NDE of components manufactured using advanced manufacturing technologies (AMT). The workshop, focused on NDE for the commercial nuclear power industry, was attended by participants from the U.S. and abroad including representatives of academia, industry, and government laboratories. Overall, the workshop showed that the NDE community is proactively addressing key issues in inspection of AMT materials, with strong foci on topics that affect inspectability, including flaw detection, surface conditioning, and material properties.

# Acronyms and Abbreviations

| | |
|---|---|
| ADAMS | Agencywide Documents Access and Management System |
| AI | artificial intelligence |
| AMT | advanced manufacturing technology |
| ASME | American Society of Mechanical Engineers |
| CT | computed tomography |
| DED | directed energy deposition |
| DMAS | delay-multiply-and-sum |
| EBW | electron beam welding |
| EPRI | Electrical Power Research Institute |
| ET | eddy current testing |
| FMC | full matrix capture |
| HAZ | heat affected zone |
| HIP | hot isostatic pressing |
| ISI | inservice inspection |
| IQI | image quality indicator |
| LOF | lack of fusion |
| LOP | lack of penetration |
| LPBF | laser powder bed fusion |
| ML | machine learning |
| NDE | nondestructive evaluation |
| NRC | U.S. Nuclear Regulatory Commission |
| PCRT | process compensated resonance testing |
| PE | pulse-echo |
| PM | powder metallurgy |
| PNNL | Pacific Northwest National Laboratory |
| RT | radiographic testing |
| RUS | resonant ultrasound spectroscopy |
| TFM | total focusing method |
| TOFD | time of flight diffraction |
| UT | ultrasonic testing |
| WAAM | wire arc additive manufacturing |

# Contents

# Figures

# Tables

# 1.0 Introduction

Advanced manufacturing technologies (AMTs), including electron beam welding (EBW), powder metallurgy (PM) hot isostatic pressing (HIP), and additive techniques such as laser powder bed fusion (LPBF) and wire arc additive manufacturing (WAAM), are of growing interest to the U.S. commercial nuclear power industry. A key step in the acceptance of AMTs in commercial nuclear power plants will be the assurance that components meet performance requirements, including those established for inservice inspection (ISI).

EBW in particular has been a focus of research by the Electrical Power Research Institute (EPRI) and others who are developing scale mockups of reactor pressure vessels using AMTs (Gandy 2020). In a July 2023 Supplementary Project Note, EPRI identified nondestructive evaluation (NDE) methods for inspecting electron beam welds as a barrier preventing EBW from being deployed across the nuclear industry (EPRI 2023a). The ISI methods that monitor component integrity need to be effective and reliable. To address issues of component inspectability, Pacific Northwest National Laboratory (PNNL) was tasked by the U.S. Nuclear Regulatory Commission (NRC) to perform confirmatory NDE research on components and mockups made using AMTs to help the NRC understand the ISI methods and techniques that will be most effective at detecting defects in AMT components. The focus of this report is on the inspectability of EBW mockups.

In brief, EBW uses high-energy electrons to melt and join materials in a butt weld without filler material. EBW is particularly attractive to the nuclear industry because it is much faster than conventional methods for joining large-scale components like reactor pressure vessels, potentially resulting in significant time and cost savings in construction. Although EBW has been around for many decades, it is considered by the NRC to be an AMT since it has not yet been utilized in a safety-critical component in a U.S. commercial nuclear plant. See section 3 of this report for a brief introduction to EBW, including some types of flaws or defects that can occur. For more in-depth information on EBW for the nuclear power industry, a comprehensive review was provided to the NRC by Oak Ridge National Laboratory (Faraone et al. 2022).

As an example of the rapid pace at which the nuclear industry is advancing with EBW technology, in February 2024, Sheffield Forgemasters released a statement that they had assembled a full-size small modular reactor nuclear vessel demonstrator using EBW.[1] The wall thickness of the 3 m diameter demonstrator was 200 mm, and the welding process was completed in under 24 hours. The statement said that the weld had no defects and that the EBW technology "reduce[s] the need for weld inspections because the weld joint replicates the parent material." Faraone et al. (2022) stated that the long-term goal is to eliminate ISI of heat-treated EBW joints.

The American Society of Mechanical Engineers (ASME) Boiler and Pressure Vessel Code outlines requirements for inspection of Code class weld joints. Most inservice NDE methods were developed for inspecting conventionally manufactured components. Whether existing methods will be appropriate for inspecting AMT components is an open question. The confirmatory research of this project is focused on determining the appropriate ISI methods that will allow EBW defects to be reliably detected to allow AMT components with EBW to be incorporated into plants. Prior to initiating confirmatory research, PNNL conducted a literature

[1] https://www.neimagazine.com/news/sheffield-forgemasters-completes-smr-nuclear-vessel-demonstrator-11533660. Accessed 30 May 2024.

search in 2020 and a gaps-analysis on NDE of AMT materials with a focus on nuclear industry ISI (Jacob et al. 2020). Then, in 2023, the NRC and PNNL jointly organized the first public workshop on NDE of AMT to obtain more contemporary information. Nuclear industry stakeholders from utilities, academia, national laboratories, and other organizations from the U.S. and abroad gave presentations and participated in discussions on the inspection challenges posed by AMT materials. A summary of the workshop is given in section 2.

The remaining sections of this report focus on NDE of butt-welded EBW mockups. Important introductory terminology and concepts are given in section 3, where the EBW defect types and the merits and potential shortfalls of different ultrasonic testing (UT) approaches are illustrated. Four mockups were studied, and each was welded with unique EBW parameters to produce a variety of weld defects. The mockups are described in section 4, and the NDE methods used are described in section 5. The results of radiographic and ultrasonic NDE are described in section 6, including UT data acquired pre- and post-heat-treatment.

# 2.0 NDE of AMT Workshop Summary

On May 2-3, 2023, the NRC hosted a workshop to facilitate the exchange of technical information focused on the state-of-the-art of NDE of AMT components in the nuclear industry, as well as key challenges associated with the use of these technologies. To our knowledge, this was the first workshop focused entirely on NDE in additive manufacturing. The two-day meeting was attended in-person by over 20 U.S. and international stakeholders, and at least 80 online attendees joined for at least some of the meeting. The meeting included presentations from representatives in academia, research laboratories, the nuclear power industry, and government agencies working on addressing key NDE challenges in AMT. During the meeting, the audience actively engaged in discussing a wide range of AMT NDE topics.

For those authors who agreed to have their presentation made public, the presentation files were combined into a publicly available package for NRC's ADAMS[1] database with ADAMS Accession Number ML23122A125. Within that package, each presentation was assigned its own Accession Number. The authors, abstracts, and individual Accession Numbers are provided in Appendix A.

Following the workshop, we reviewed the presentations for recurring themes, and tabulated the themes according to the number of different presentations that the theme occurred in. We then reviewed the recent PNNL report (Jacob et al. 2020) that identified and ranked gaps in NDE of AMT. Each theme from the meeting was correlated to a gap in the report. The information presented at the workshop was contemporary, whereas the gap report was published several years prior and was based on publications (the information in publications is often a year or two old by the time a manuscript goes to press). As NDE of AMT is a rapidly emerging research topic, we were interested to see how NDE priorities in AMT may have evolved based on the most recent information received from the workshop. All the workshop themes corresponded to medium- or high-ranked gaps in the report with the majority corresponding to high-ranked gaps, suggesting that many of the key issues in AMT component inspection identified in the report are persistent and unresolved.

Table 1 provides a high-level summary of the recurring themes listed in descending order of the frequency they were found in the workshop presentations. The ranking of the corresponding gap identified in (Jacob et al. 2020) is given (M = medium, H = high). Note that abbreviations in the table are defined at the bottom of the table. More comprehensive information can be found by referring to the presentations in ADAMS (ML23122A125).

[1] ADAMS, the Agencywide Documents Access and Management System, is the official recordkeeping system of the NRC. Documents posted in ADAMS are publicly available. https://www.nrc.gov/reading-rm/adams.html. The Accession Number is a document identifier that can be used to search for specific records.

Table 1: Recurring Themes and Issues Identified at the Workshop Correlated to the Gap Ranking Identified in Jacob et al. 2020.

| Theme | Issues Identified | Gap Ranking |
|---|---|---|
| Flaws (flaw detection, flaw types, critical flaws) | CT porosity detection is slow, is affected by contrast-to-noise ratio, and finds pores that are not critical flaws. UT resolution too low. Discerning between defects, indications, and noise is difficult. Many flaws are detected in WAAM, but none are "rejectable indications," although there is currently no definition of what constitutes a rejectable indication. Porosities significantly change acoustic impedance even in >99% dense parts. Correct flaw sizing is a challenge. | M |
| Surface condition | Surface roughness causes poor UT coupling, UT sound scatter, poor ET results from lift-off variance. NDE needs a machined surface. | H |
| Gaps, needs, paths forward | Multiple gap analyses have been written, and they should be aligned. Standardization is needed. There was a call for a national testbed facility or user facility. | H |
| Material properties (characterization, grain structure, microstructure) | Characterizing materials results in large data sets with low throughput. There needs to be a better understanding of microstructure and effects on material properties and spatial variability. The effects of microstructure on UT at different scales, relevant frequencies, and beam sizes need to be characterized. RT in lieu of UT may be feasible. Correlate microstructure to UT signals. | H |
| Reference standards, calibration standards, procedures | Standards are critical for RT and CT scans. Adding well-characterized flaws to a build is needed, but many times there are distortions in intended flaws. | M |
| NDE validation | Validation can relate UT to porosity and process anomalies. CT can be used as a reference method. Correlate RUS/PCRT to material conditions. | H |
| Part variability | Printing equipment turnover results in potentially different builds. Build-to-build variations need to be minimized or accounted for. Identify causes of random defects. | H |
| Qualification of parts | Critical build parameters should be determined and microstructure characterized. Appropriate witness coupons are needed. Qualification should be process driven. Acceptance criteria need to be defined. | M |
| Part complexity | CT is a reference NDE method for complex parts. Conformable UT probes may help with complex geometries, but in general UT is not suited to complex parts. | M |
| Flaw/defect formation and/or propagation | Fatigue is a major issue for AMT components. "Effect of defect" analysis is needed. | H |

| Theme | Issues Identified | Gap Ranking |
|---|---|---|
| Inservice inspections | Inservice inspections will be needed for some components. | H |
| AI/ML | AI might be used to train NDE to identify acceptable parts, identify flaws, and improve CT reconstruction. Training data will be needed. | M |
| Table Abbreviations:<br>AI: artificial intelligence<br>CT: computed tomography<br>ET: eddy current testing<br>ML: machine learning<br>PCRT: process compensated resonance testing<br>RT: radiographic testing<br>RUS: resonant ultrasound spectroscopy<br>UT: ultrasonic testing<br>WAAM: wire arc additive manufacturing | | |

Table 1 shows that the topic of flaw detection emerged as the most frequently discussed theme in the workshop. In the gap report, this topic was ranked as medium because the report authors concluded there were many ISI issues that needed to be addressed before flaw detection could even be considered. However, this workshop suggests that the NDE research community is strongly focused on flaw detection, with outstanding questions remaining, such as: what are critical flaws that may result from the build process, where are such flaws located, and how can current NDE technology be used to identify them? The difference in the flaw detection priority (i.e., medium in the report versus the most frequent theme of the workshop) may reflect recent advancements in understanding the types and locations of flaws that occur during the AMT build processes.

Surface condition was also recognized as an important topic in both the report and workshop. Additive manufacturing processes—those that use powder or wire—tend to leave a surface with roughness on the order of the size of the constituent material. Surface conditions adversely impact most NDE techniques. For example, rough surfaces reduce coupling between the UT probe and part surface, scatter ultrasonic energy, create liftoff of eddy current probes, and cause artifacts in radiographic images. Solving the surface condition problem will require innovations in the build processes, innovations in NDE techniques, or post-build surface conditioning.

Other recurring themes included validating and standardizing NDE methods, coordinating research efforts to solve difficult problems, aligning gaps across industries, developing measurement and calibration standards that accurately reflect microstructures and material properties, and dealing with part complexity. In short, workshop attendees recognized that a lot of work will be required for NDE to catch up with the rapid progress being made in AMT.

Interestingly, there was an unexpected workshop focus on resonant ultrasound spectroscopy (RUS) for microstructural and material characterization. During RUS, a transmitting transducer on a specimen is swept through a range of frequencies. Resonant peaks at the specimen's natural frequencies are recorded by a receiving transducer. The positions, widths, and intensities of the peaks are analyzed to determine the specimen's elastic properties. RUS is useful for understanding material characteristics, particularly on small, geometrically regular samples. However, application of RUS in nuclear ISI of large components is unlikely, and RUS was not mentioned in the report as a potential inservice NDE modality.

Some gaps that were ranked as high in the report were not discussed much in the workshop. These are topics of special interest to the nuclear industry but are not being prioritized by the NDE community at large, such as ISI, degradation mechanisms, and defect formation or propagation. The nuclear industry lags many other industries in the acceptance of AMT materials, so there has not been much effort and research put toward understanding inspection issues specific to the industry. The lack of focus on ISI is understandable because we do not yet know which AMT components will require inspection nor what they will be inspected for. However, we still consider the gaps corresponding to these topics to be ranked as high because they must be addressed prior to installation of such components. Indeed, as the nuclear industry gets closer to deploying a safety-critical AMT component, ISI issues will come to the forefront. Any ASME Code actions that will be required for Section XI[1] may take months or years, potentially slowing down the process of deployment.

One issue that emerged in the workshop was that there are significant difficulties in determining essential variables and ideal parameters that are reliably repeatable from one AMT build to the next, at different sites, or using different equipment. In fact, build variability was mentioned several times in the workshop and was recognized as a high-ranking gap in the report. Developing NDE methods on a moving target is problematic; until build parameters are determined, demonstrated, and standardized, applying NDE to test objects may be premature. For example, the NRC considers PM-HIP to be an AMT. Although it is an active area of research by nuclear industry stakeholders (EPRI 2023b; Gandy 2015; Gandy 2021), we have found that PM-HIP is rarely included in discussions in the AMT community. The ideal HIP parameters and powder characteristics must be determined before building a PM-HIP component that meets Section III[2] criteria. Until such time, there is obvious reluctance to spend resources developing NDE techniques to inspect PM-HIP test objects that may not meet Section III standards. In addition, there is a need for PM-HIP facilities that can fabricate large, pressure-retaining components used in nuclear plants. There are currently no facilities that can PM-HIP a seamless full-scale, or even 2/3 scale, upper head for a small modular reactor. Such facilities are being conceived and designed (Hoelzer 2022; EPRI 2016), but until they can be constructed, tested, and demonstrated we anticipate a lack of large-scale nuclear-relevant PM-HIP components for NDE testing and development. In the meantime, smaller components, such as valve bodies, are being built and tested using wire directed energy deposition (DED) (Melfi 2023). Smaller components can be built and tested relatively quickly and cheaply, meaning that essential variables and parameters can be determined more rapidly. Even so, DED components must still ultimately comply with Section III requirements.

Overall, the workshop showed that the NDE community is proactively addressing key issues related to the inspection of AMT materials. A second workshop with similar themes was held in April 2024 at EPRI.

---

[1] American Society of Mechanical Engineers (ASME) Boiler and Pressure Vessel Code (BPV Code, or Code) Section XI, *Rules for Inservice Inspection of Nuclear Power Plant Components.*

[2] American Society of Mechanical Engineers (ASME) Boiler and Pressure Vessel Code (BPV Code, or Code) Section III, *Rules for Constructions of Nuclear Facility Components.*

# 3.0 Terminology and Concepts

## 3.1 Electron Beam Welding

Electron beam welding is a welding technique that uses a beam of high-energy electrons to melt and join components without the use of filler material, such as brazing rods or wire electrodes (Kim et al. 2016). Without filler material, abutting faces must be machined to close tolerances, resulting in a smooth, planar joint line.[1] Figure 1 illustrates the process. The beam melts and vaporizes the metal forming a keyhole while the surrounding metal forms a melt pool. As the beam is translated along the joint line, the melt pool fills the keyhole and fuses the base metals together forming a weld. The EBW process leaves a small heat affected zone (HAZ), and the resulting weld joint is narrow when compared to a typical V or double-V weld in conventional welding. For example, figure 2 shows photographs of an electron beam weld from this study compared to a conventional dissimilar metal weld from a mockup of similar thickness, described in (Jacob et al. 2019). The melt zone and HAZ of the EBW are clearly visible. There are narrow bands of predominantly horizontal grain microstructure between the two zones with somewhat larger grains than are visible in the melt zone or HAZ. The top of the weld near the crown is flared, but the rest of the weld is straight with a melt zone that is only a few millimeters wide. The total width of the EBW weld region is about 10 mm. By comparison, the V weld has larger grains with greater variation in grain orientation, and the width of the V weld is about 40 mm at the weld crown and about 30 mm at half the specimen thickness.

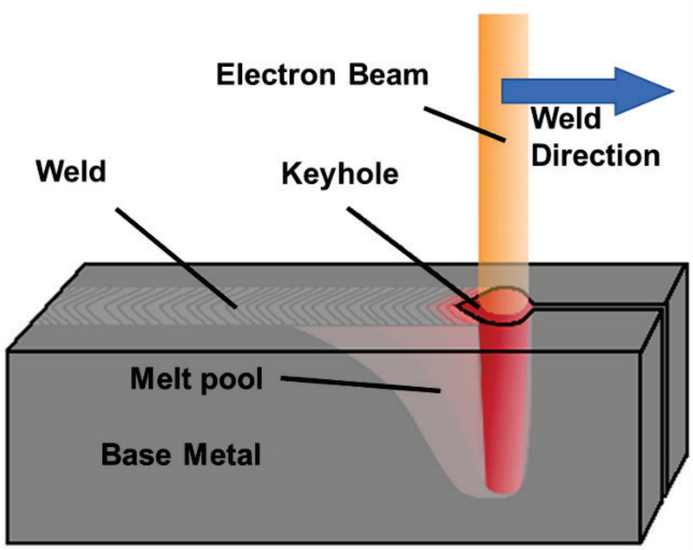


Figure 1: An illustration of electron beam welding.

[1] In EBW, “joint line” refers to the line or plane where the base metals meet. In conventional welding, “fusion line” refers to the line along which the filler metal and the base metal meet.

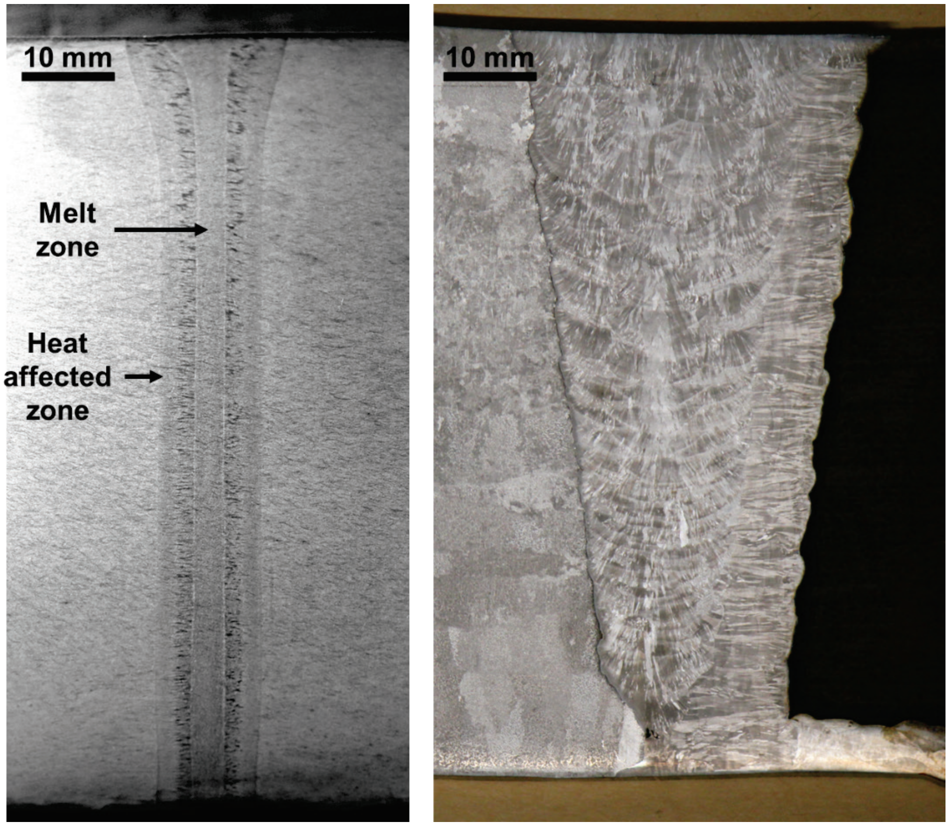


Figure 2: Comparison of EBW and conventional dissimilar metal weld profiles. The left photograph shows a profile from a mockup in this study. The right photograph shows a profile from a cast austenitic stainless steel to carbon steel dissimilar metal weld.

Defects in electron beam welds may include lack of penetration (LOP), lack of fusion (LOF), weld metal cracking, gas porosity, residual stress, and voids or cavities caused by a sudden increase in beam penetration (Cottrell 1985). Defects relevant to this report are discussed in section 3.2. Because no filler material is (typically) used in EBW, post-weld heat treatment can cause the microstructure of the weld region to match the microstructure of the parent material (Gandy and Stover 2018). The impact of heat treatment on UT will be discussed in section 6.3.

## 3.2 EBW Defect Types

There are three types of EBW defects that are relevant to this report: keyholes, LOF, and LOP.

### 3.2.1 Keyhole Defect

A keyhole is formed when the electron beam vaporizes the base material and melts the surrounding material. The keyhole is typically filled as the beam moves forward and the molten metal flows into the void. During the welding process of block 2, a beam shutdown left an unfilled void, or a full-thickness keyhole defect.

### 3.2.2 Lack of Fusion

An LOF defect occurs when the electron beam is not steered properly or is misaligned and misses the joint line. The beam is focused and steered with magnetic coils, or "lenses," and improper setting of the lenses can lead to such defects. LOF defects can be partial or full thickness, as illustrated in figure 3. Panel A shows an ideal weld, with the fusion zone encompassing the entire joint line and penetrating the full depth of the material. Panel B shows the effects of poor beam alignment; almost the entire joint is missed resulting in a nearly full-thickness LOF. Panel C shows an error in beam steering that causes a partial LOF. Block 2 had a small region with a partial LOF (such as shown in panel C), and block 3 had a large region of LOF spanning nearly the full thickness (such as shown in panel B).

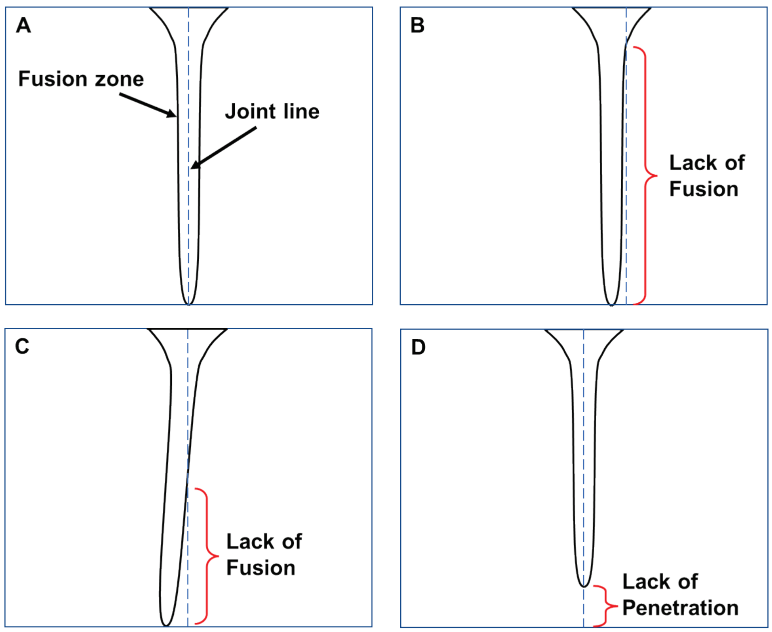


Figure 3: An illustration of lack of fusion and lack of penetration defects. A: This is an ideal weld where the fusion zone entirely encompasses the joint line. B: Misalignment of the beam can result in a full-thickness or nearly full-thickness lack of fusion. C: Misdirection of the beam can cause a full-thickness or partial-thickness lack of fusion. D: A lack of penetration defect can result from poor beam settings.

### 3.2.3 Lack of Penetration

An LOP defect is illustrated in figure 3, panel D. This type of defect occurs when the full thickness of the material is not penetrated by the beam due to low beam power, poor beam focusing, or poor beam manipulation (the beam can be manipulated or steered in a variety of patterns depending on the application to increase or shape the melt pool region; see (Tao et al. 2022)). Block 4 in this report had an LOP defect along the full length of the joint line. An LOP defect is visible due to the lack of a weld root.

## 3.3 Ultrasonic Testing Methods

In EBW, LOF and LOP defects are flat, vertical, and smooth surfaces, unlike defects that may occur in a conventional V weld, so the UT approach to detecting and characterizing such defects may need to be varied from the conventional pulse-echo approach. Several different UT methods were used in this work to examine the EBW weld joints. Brief descriptions of these methods are given below.

### 3.3.1 Full Matrix Capture

Full matrix capture (FMC) is an advanced UT method that utilizes an array probe and sequential element pulsing. This method is described in detail in (ASME 2023). In brief, ultrasonic energy is transmitted by pulsing each element of the array one by one while the entire array is used for reception. If there are N elements of the array, then N waveforms are received after each element is pulsed. The result is N×N total waveforms are received at each scan position. By applying different time delays to each A-scan during reconstruction, every beam angle and focal depth can be calculated. Thus, the key advantage of FMC is that an image can be reconstructed that is focused at every position within the specimen, which can provide improved resolution and signal-to-noise ratio over conventional UT methods. The main disadvantages of FMC are that the N×N waveforms at each position make the file sizes large and acquisition times long. FMC can also suffer from lack of energy transmitted into the part due to the small (single array element) transmitting aperture; this can be a significant problem in attenuative materials such as austenitic welds, but FMC is well-suited for carbon steel materials such as the EBW blocks used in this report. FMC can be performed in pulse-echo (PE) mode using a single array probe for transmitting and receiving or in pitch-catch mode using separate array probes for transmitting and receiving. For the current work, PE mode was used.

Unfortunately, there are problems with applying PE UT to the EBW mockups in this work, whether using FMC or conventional UT. The joint lines are smooth, vertical planes, as opposed to traditional V welds that have fusion lines that are angled with respect to the specimen surface. When using PE to inspect the EBW joints, a corner trap, or surface-connected portion of a flaw, can be readily detected but the flaw depth cannot. Figure 4 illustrates the issue. In the top panel, the transmitted signal (blue arrow) is incident on a flaw along the fusion line in a V weld, and the reflected signal (green arrow) is received at the probe. Thus, the flaw can be detected with PE when the appropriate refraction angle is used. By moving the probe, an inspector can depth-size the flaw based on the echo intensity and probe position or by detecting a tip-diffracted signal. The bottom panel shows a vertical joint line with the transmitted signal (blue arrow) reflected away from the probe, which occurs for every probe position except when sound impinges the corner. Thus, depth sizing is impossible unless a tip diffracted signal is detected. In this same scenario, sound that traverses through a fused weld joint will also not return to the probe. Therefore, unless a corner-trap echo is detected, bonded and unbonded EBW joints will have the same ultrasonic signature.

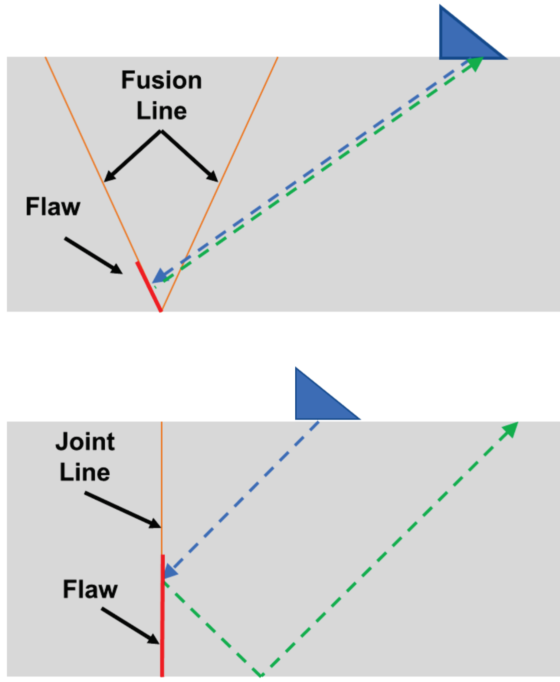


Figure 4: Illustration of pulse-echo UT for a conventional V weld (top) and an electron beam weld (bottom). Transmitted and reflected sound paths are shown with blue and green arrows, respectively.

### 3.3.2 Time of Flight Diffraction

Time-of-flight diffraction (TOFD) is a pitch-catch UT method in which the probes are arranged to face each other from across the weld at a fixed separation, as shown in figure 5. Typically, this method is used to obtain tip-diffracted signals to enable flaw depth sizing, especially for embedded flaws. In this report, we used a TOFD-like setup because of the planar weld joint geometry and the difficulties that such a geometry poses to standard pulse-echo UT. When using TOFD with the EBW weld geometries, the receiving probe (R) will pick up the ultrasonic energy (blue arrow) from the transmitting probe (T) unless the sound path is blocked by an unfused interface, in which case the sound will be reflected away (red arrow). Thus, by moving the probes together with respect to the joint line, both detection and sizing are possible. Conventional TOFD uses single-element probes. However, an example of a pitch-catch FMC setup is in (Nicolson et al. 2024), where they inspected narrow-gap welds. Like EBW joint lines, these welds have smooth, vertical surfaces, but they have a larger gap than those of EBW joints. Nicolson et al. showed that the pitch-catch setup increases sensitivity and effectiveness of the inspection versus using a single probe.

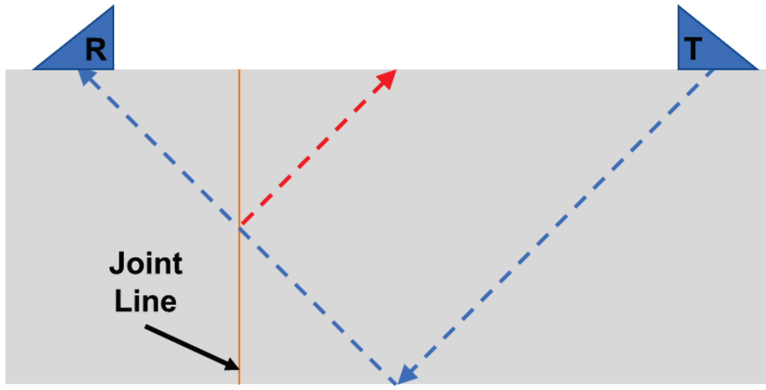


Figure 5: Illustration of time-of-flight diffraction UT. The receiving probe (R) will pick up the ultrasonic energy (blue arrow) from the transmitting probe (T) unless the sound path is blocked by an unfused interface, in which case the sound will be reflected away (red arrow).

Because of the inherent symmetry of the TOFD setup, it is not strictly necessary to move the probes across the full width of the specimen. Figure 6 shows two different probe positions, red and blue. The signal received by the blue probes is theoretically equivalent to that received by the red probes. At the red and blue positions, the sound energy must traverse through exactly the same point in the joint line and must travel the same distance through the material. In practice, differences in signal are caused by beam spread (i.e., between the blue probes, the beam would spread more before encountering the weld than with the red probes), spatial variations in backwall surface roughness, backwall geometry, fluctuations in probe coupling, or material property differences (such as in a dissimilar metal weld).

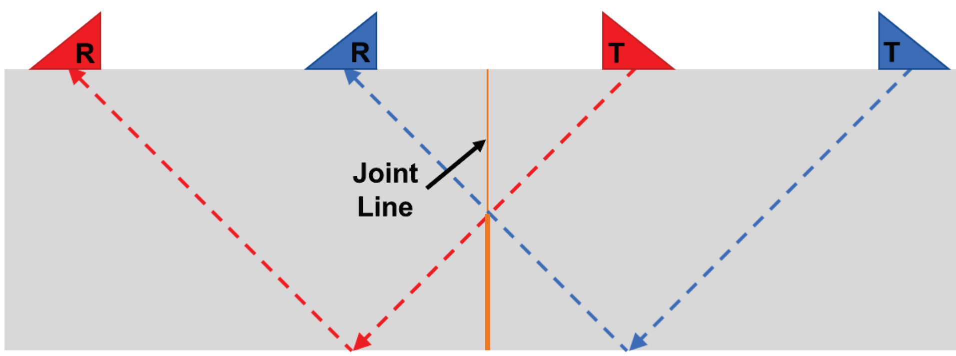


Figure 6: Illustration of symmetry in TOFD. For both the red and blue probes, the sound path, indicated by the arrows, must traverse through the same point in the weld and travel the same distance through the material. Thus, the received signal should be theoretically identical. R and T indicate receiving and transmitting probes, respectively. Due to coverage limitations, only a portion of the joint line can be inspected, shown by the bold portion of the joint line.

When using TOFD, the probe separation is a function of the inspection depth and the refraction angle. For 45° refraction angles, we fixed the probe separation at twice the specimen thickness so that a direct backwall echo could be detected (note that for conventional TOFD the probes are not usually spaced this far apart). If the distance between the joint line and the edge of the mockup is less than the probe separation, then the probes cannot be moved far enough back to fully cover the weld. For example, in figure 6, the blue T probe is at the right edge of the specimen, but the sound energy is only passing through the middle of the joint line. As the probes are translated to the left, the sound will traverse through lower and lower portions of the joint line. When the midpoint between the probes reaches the joint line, the base of the joint will be insonified. Then, as the probes are moved further to the left, the sound will traverse through higher and higher portions of the joint line until the R probe reaches the other edge of the mockup (as shown in red). The portion of the joint line that is ultimately being covered (twice) by the inspection is shown with a bold line. In this work, the specimens were 90 mm thick but the distance from the welds to the edge of the plates was only 150 mm. A single TOFD scan could not provide full coverage, so to cover the full joint line the plates were scanned from the top and bottom surfaces.

### 3.3.3 Tandem

Tandem is a pitch-catch UT method in which the probes are arranged one behind the other and facing the same direction.[1] This arrangement allows the probes to be on the same side of the weld if there are coverage limitations while potentially avoiding some of the difficulties that the EBW joint line geometry poses to standard PE. However, only echoes from flaws of a specific depth will be detected, and that depth depends on the probe separation. Figure 7 illustrates two probes in a tandem configuration, where an echo will be received if the transmitted sound is incident at a certain depth (left) but not if the sound is incident at another depth (right). However, unlike the idealized pencil beam drawn in figure 7, beam spread expands the sound field and increases the region of sensitivity. Notably, tandem will not be sensitive to corner-trap echoes unless the probe spacing is smaller than or comparable to the beam spread. That is, corner echoes *might* be detectable if the probes are close enough together. For tandem to be sensitive to a range of flaw depths, a dynamic approach is required in which the probe spacing can be varied. This is an uncommon technique that requires specialized fixturing and encoding.

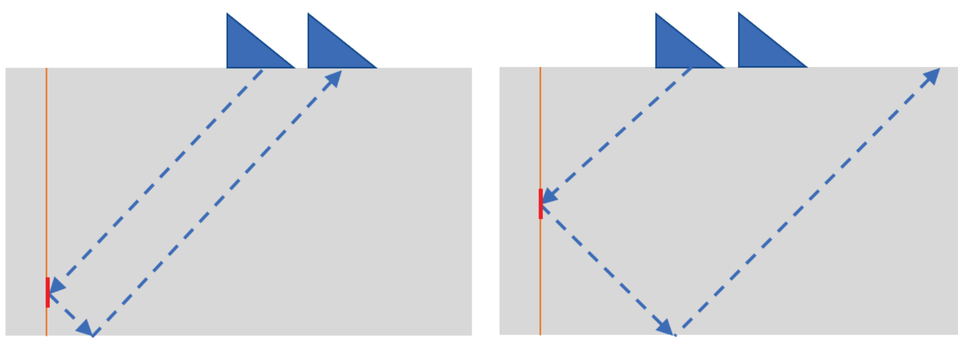

Figure 7: Illustration of tandem UT. Flaws of a certain depth can be detected with specific probe spacing, as in the left panel. Flaws of another depth cannot be detected with the same probe spacing, as in the right panel.

[1] To minimize surface waves and other spurious signals from being picked up by the receive probe, we suggest using the front probe as the transmit probe.

# 4.0 Descriptions of Mockups

Four EBW blocks were loaned to PNNL by EPRI. The blocks were fabricated at the Nuclear Advanced Materials Research Centre in Sheffield, U.K. They were made from a single billet of forged ASTM/ASME SA508 Grade 3 Class 1 carbon steel. This type of steel is commonly used in pressure vessel, steam generator, and pressurizer applications in the nuclear industry (Mandal et al. 2020). Each block comprised two machined sections, one was approximately 500 mm × 150 mm × 100 mm and the other was approximately 500 mm × 150 mm × 90 mm. Figure 8 shows an end view of a welded block.

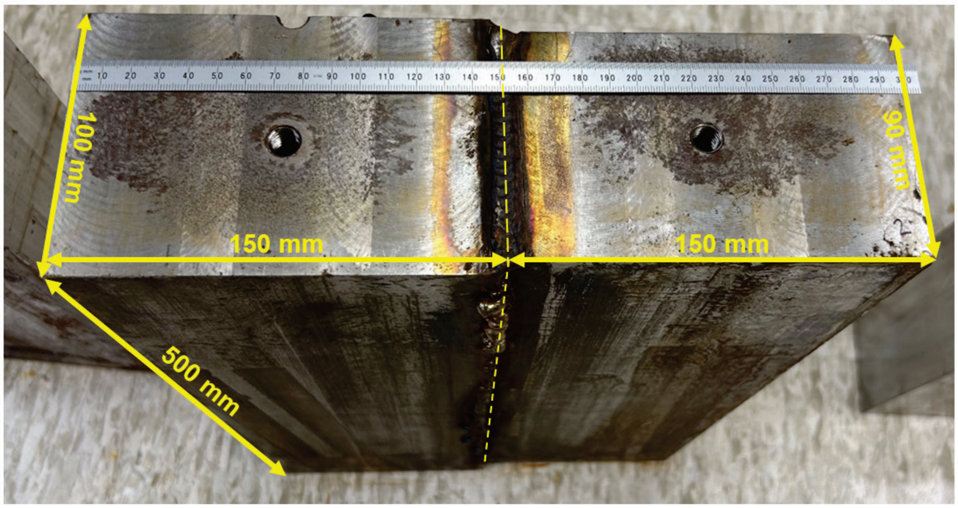


Figure 8: End view showing the block dimensions. The dashed line indicates the weld joint. The holes on the end of the block are to accommodate lifting bolts.

The blocks were joined with a simple square butt weld. The welded faces were machined smooth and planar, and the blocks were held tightly together with tack welds in preparation for the EBW process. The electron beam was 450 mA and 60 kV with a welding speed of 2 mm/s. The distance from the electron source to the component was 400 mm. During EBW, the beam is typically oscillated back-and-forth (across the joint line) and/or front-to-back (along the joint line) to distribute the beam energy; different oscillation patterns are used depending on the welding parameters and the desired outcome. The beam was oscillated by 3 mm along weld direction and 1 mm perpendicular to the weld direction at a frequency of 501 Hz, except for block 4 where the axes of oscillation were intentionally reversed to induce an LOP defect.

The side of the block where the beam entered was the crown side, and the opposite side was the root side. In this report, the crown side of the block is referred to as the top of the block and the root side as the bottom.

After we completed the RT and FMC UT, we received permission from EPRI to machine smooth the top and bottom surfaces of all four blocks to facilitate additional UT scanning. The blocks were machined to 90 mm thick (about 5 mm were taken from the top and bottom of the 100 mm end), and the weld crown and root were removed. We also received permission to cut a ≈50 mm section off the end of block 1 for metallography and heat treatment (section 6.3). The cut face of the section was polished and chemically etched to reveal the weld profile, as shown in figure 2. The TOFD and tandem scans were performed after machining.

## 4.1 Weld Characterization

To characterize the welds, we performed 0° encoded UT at 10 MHz from the side of the blocks (the UT method is described in section 5.2.2). Figure 9 illustrates that if the sound energy is reflected by an unfused weld, the echo received is relatively strong, as shown by the thick red arrow. If sound energy passes through a fused weld, then the echo received is relatively weak due to the longer metal path, as shown by the thin green arrow. Therefore, LOF and LOP defects should be easily characterized by the 0° UT. One shortcoming of the 0° UT is that beam distortion is seen when the probe is too close to the edge of the specimen; therefore, we left a ~10 mm buffer zone around the perimeter of the block. Any surface-connected defects smaller than about 10 mm would not be visible. The 0° UT was performed after the blocks were machined smooth. The 0° UT images shown below in sections 4.2 through 4.5 are with the same total gain. We note that destructive testing would be the ideal method for characterizing the defects, but such testing was not performed as part of this work.

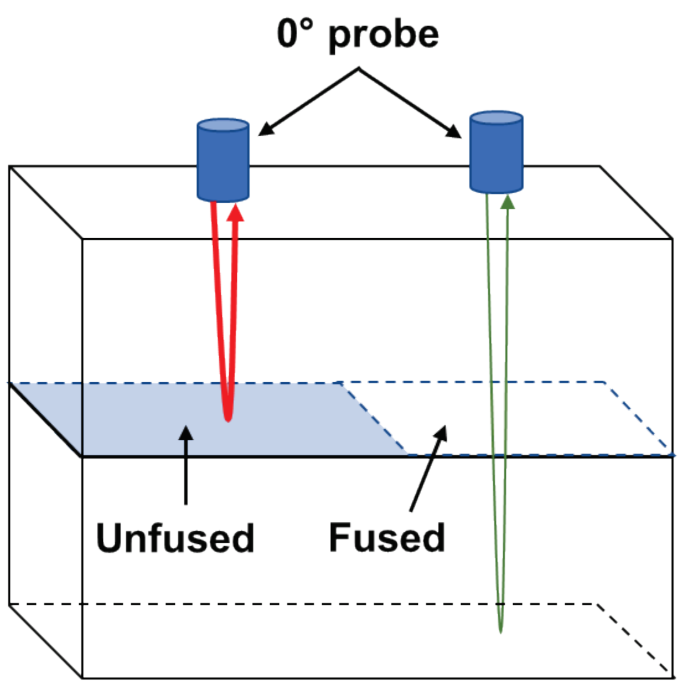


Figure 9: Illustration of the 0° UT setup. The red arrow shows a relatively strong echo from the unfused region, and the green arrow shows a weaker echo from the far side of the block when the weld is fused.

## 4.2 Block 1

Block 1 was welded with the correct EBW parameters and settings resulting in a defect-free weld. Figure 10 shows the weld crown and root, including closeups of the crown and root. The weld crown was generally smooth compared to the root, which was characterized by coarseness and splatter, normal for EBW.

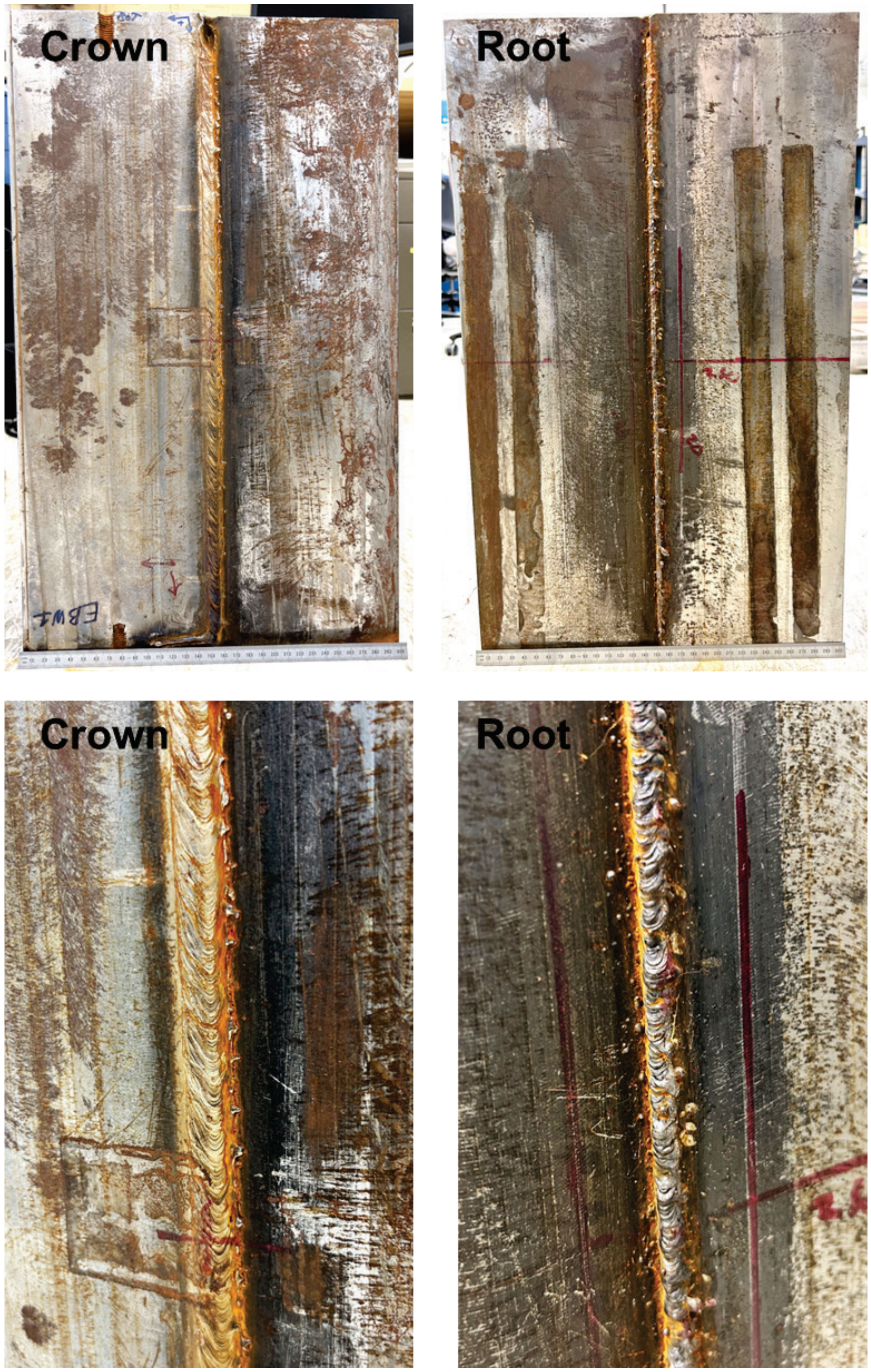


Figure 10: Photographs of the block 1 weld crown and root. The top photographs are of the whole block face, and the bottom photographs are closeups.

The 0° UT scan of block 1 is shown in figure 11. Overall, the UT signals were weak and relatively uniform, indicating a lack of echoes from the weld joint. Thus, this weld joint appeared to be well fused. There were several regions with signal dropout due to probe decoupling. The red asterisks indicate areas of lower signal intensity due to the holes drilled into the blocks for the lifting bolts (two such holes are visible in figure 8); these regions occurred in every 0° UT scan to some degree.

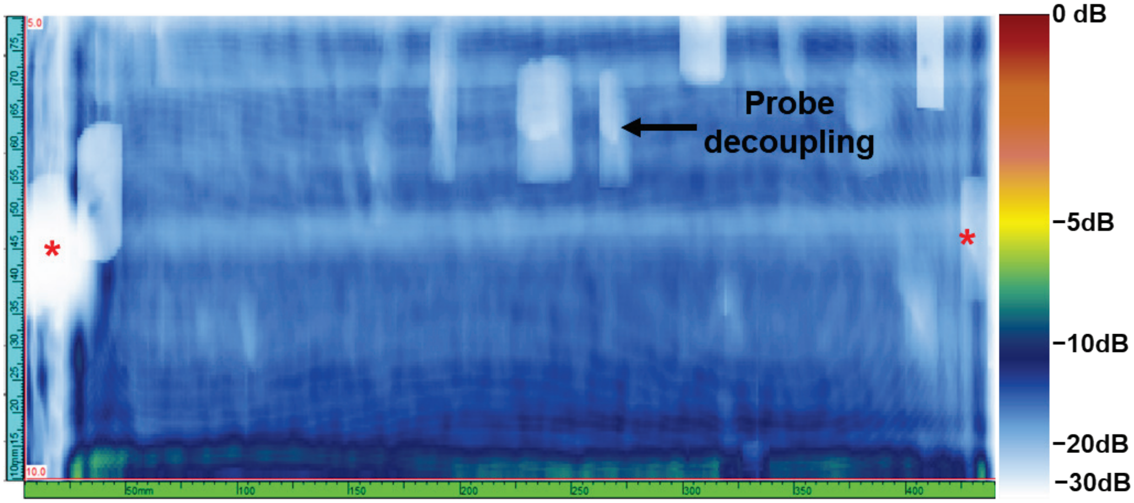


Figure 11: 0° UT scan of block 1. Overall, the UT signals were weak and relatively uniform indicating a well-fused joint. Some regions of poor probe coupling were visible. Asterisks indicate positions of lifting bolt holes. Note that the horizontal scale is compressed with respect to the vertical scale to fit the image on the page.

## 4.3 Block 2

Block 2 was welded with the same parameters as block 1. The weld crown and root of block 2 are shown in figure 12. About midway through the weld, a partial through-wall LOF flaw was created by deflecting the electron beam with a magnetic field. A slight deviation in the weld root, visible in the photographs (blue circles), was indicative of the deflected beam. A through-wall keyhole defect was also present (red ovals). This defect was caused by a beam shutdown during welding.

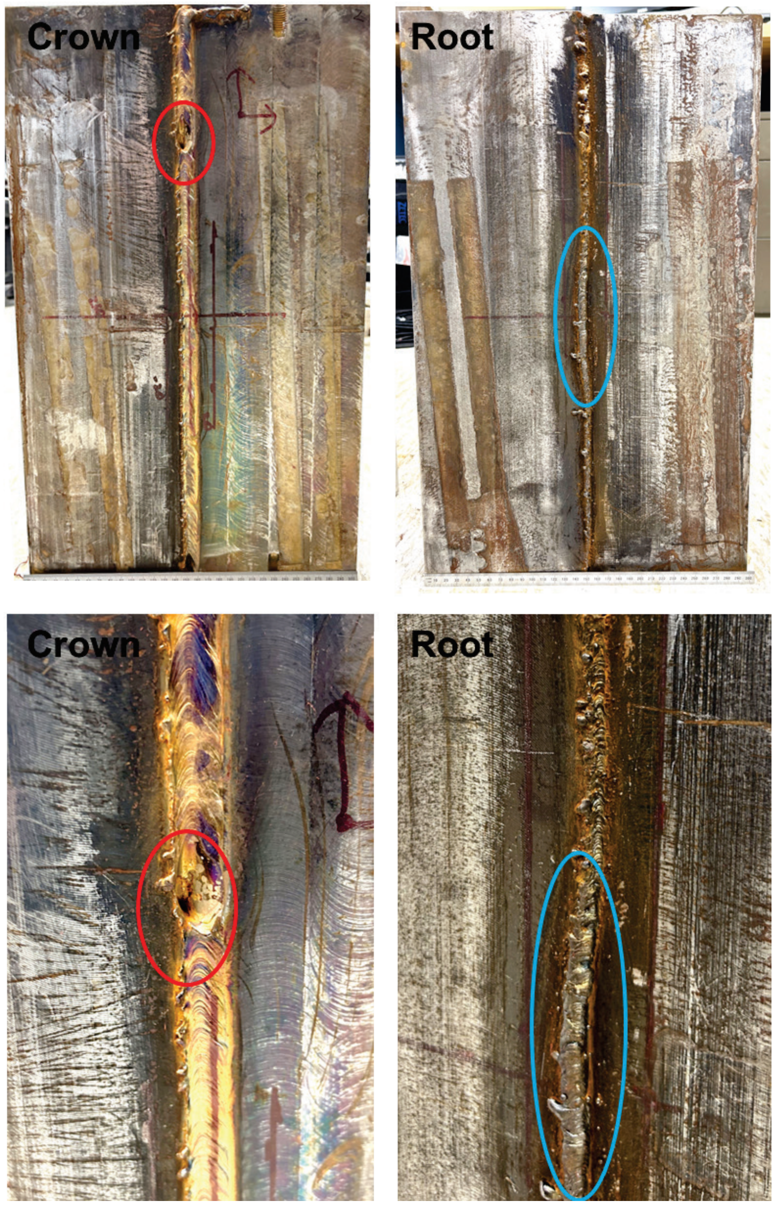


Figure 12: Photographs of the block 2 weld crown and root. The top photographs are of the whole block face, and the bottom photographs are closeups. The keyhole defect is highlighted by the red ovals and a root deviation is indicated by the blue ovals.

The 0° UT scan of block 2 is shown in figure 13. Overall, the UT signals were weak and relatively uniform, indicating a well-fused weld joint, except for the region where the electron beam was deflected and the weld joint was not fused. The keyhole defect was visible as a vertical stripe with weak signal because it scattered the sound instead of reflecting it back to the probe.

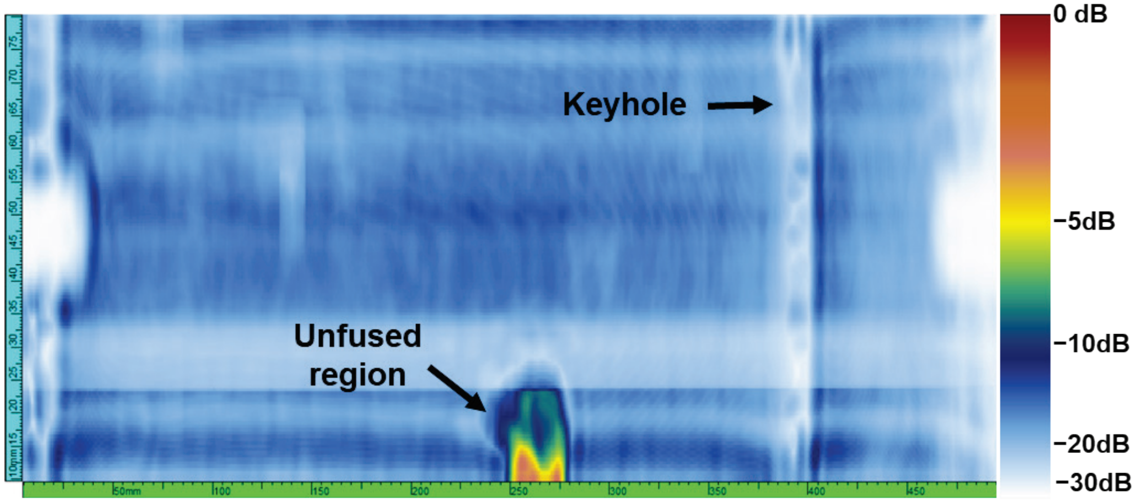


Figure 13: 0° UT scan of block 2. Overall, the UT signals were weak and relatively uniform except for the strong echo from the unfused region. Note that the horizontal scale is compressed with respect to the vertical scale to fit the image on the page.

## 4.4 Block 3

Block 3 was welded with the same parameters as blocks 1 and 2, but the beam was aligned to miss nearly the entire weld joint. Only a small region was fused; we could not visually discern the location of the fused region. A deviation was visible in the weld root (blue oval), but it was not indicative of the larger extent of the unfused region. Figure 14 shows block 3. Some rust buildup due to water couplant for ultrasonic scanning is visible in the figure.

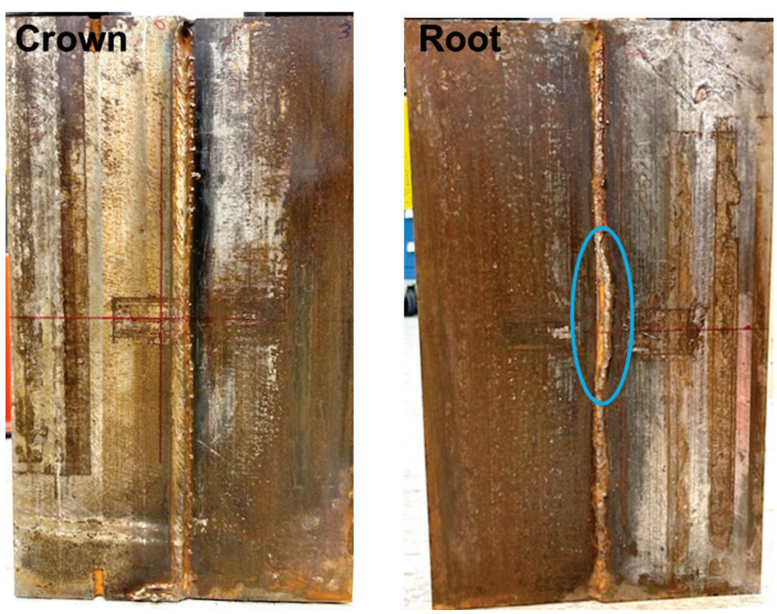


Figure 14: Photographs of the block 3 weld crown and root. A deviation of the weld root is encircled in blue.

The 0° UT scan of block 3 is shown in figure 15. Overall, the UT signals were strong, indicating most of the weld joint was unfused. There are some signal variations from the unfused surface possibly suggesting that the block surface and/or joint line was not completely smooth. There is an hourglass-shaped region where the weld appears to be well fused.

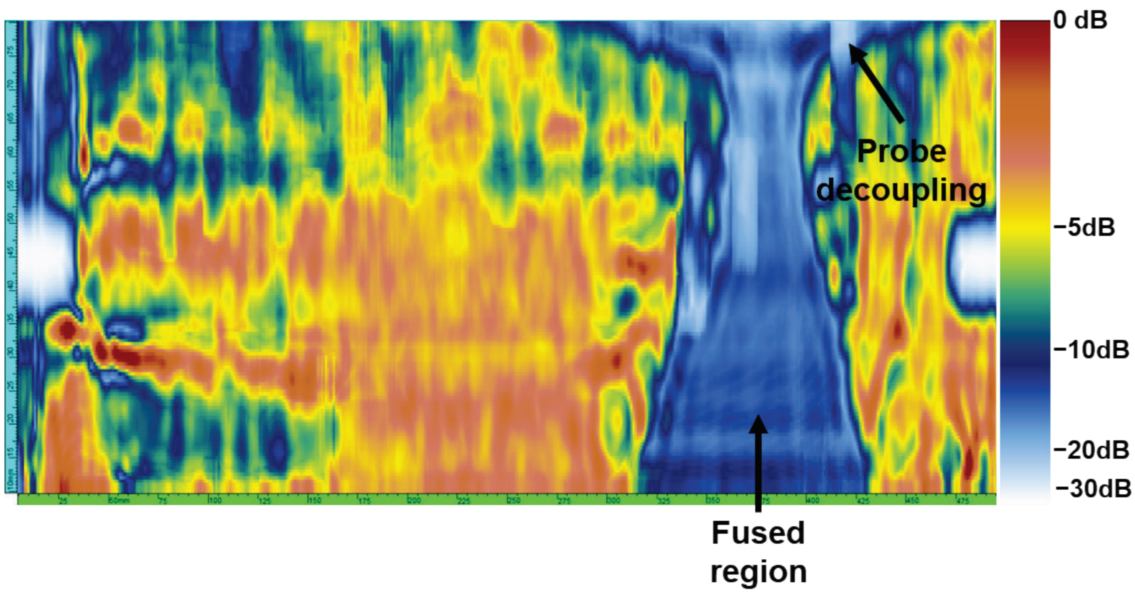


Figure 15: 0° UT scan of block 3. Overall, the UT signals were strong, indicating an unfused weld joint, except for the weak echo from the fused region. Note that the horizontal scale is compressed with respect to the vertical scale to fit the image on the page.

## 4.5 Block 4

Block 4 was welded with the same parameters as the block 1, except the beam oscillation axes were reversed. In this case, the beam was oscillated by 1 mm along the weld direction and 3 mm perpendicular to the weld direction. Because the beam spent less time in the weld direction, the melt pool did not penetrate through the entire block thickness; the result was an LOP defect along the entire length of the block. Photographs of block 4 in figure 16 show the weld root was smooth and straight with no indications of the melting or splatter seen in the other blocks, evidence that the beam did not fully penetrate the block. The depth of the LOP defect cannot be discerned visually.

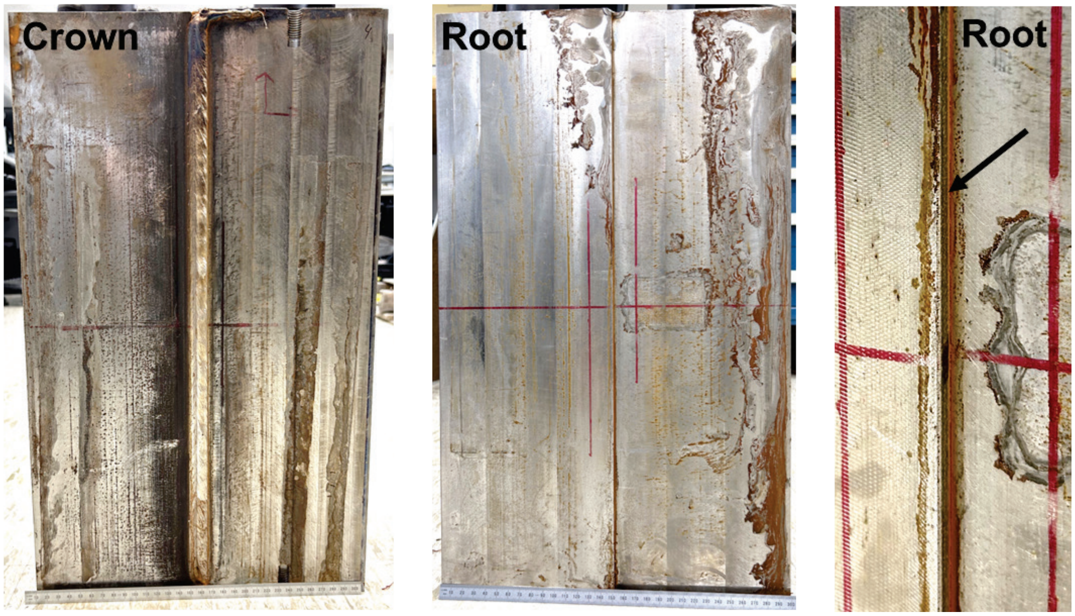


Figure 16: Photographs of the block 4 weld crown and root. The weld root appears smooth and straight. The closeup view of the root (rightmost image, black arrow) shows no melting or splatter, indicating that the electron beam did not penetrate the material.

The 0° UT scan of block 4 is shown in figure 17. Overall, the UT signals were weak and relatively uniform, indicating a well-fused joint. There are some large regions with signal dropout due to probe decoupling. The LOP defect should appear as a strong echo near the bottom edge of the figure, but it was not visible. We conclude that the LOP defect was not deep enough to be detected and is therefore ≲10 mm deep.

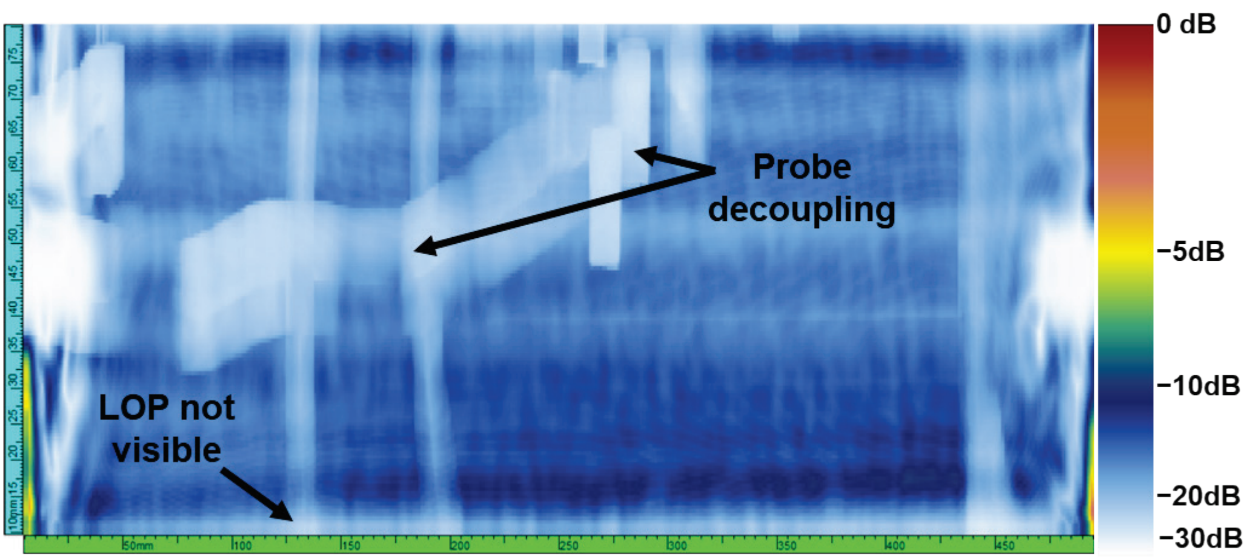


Figure 17: 0° UT scan of block 4. Overall, the UT signals were weak and relatively uniform suggesting a well-fused joint. Some large regions of poor probe coupling were visible. The LOP defect was not visible since it was within the ~10 mm buffer zone. Note that the horizontal scale is compressed with respect to the vertical scale to fit the image on the page.

# 5.0 NDE Methods

## 5.1 Radiography

Radiography was performed at PNNL to determine if it could be effective at detecting or characterizing the weld defects. The radiography system comprised a Varex 450 kV, 3.3 mA x-ray tube with a 1 mm spot size and a 2 mm thick copper plate filter. A #50 hole-type penetrameter was taped to the front of the blocks as an image quality indicator (IQI). FujiFilm SV-TI imaging plates were used for detection, and a Scan-X drum phosphor plate reader was used to digitize the images at a resolution of 40 µm. Due to the thickness of the EBW blocks and the sensitivity of the phosphor plates, each exposure took 60 minutes. With these exposure parameters, x-ray backscatter was a significant problem, so lead bricks were placed behind the phosphor plate to reduce backscatter exposure of the plate. The joint line was aligned along the x-ray beam axis. ImageJ[1] was used to visualize and analyze the images. Figure 18 shows a view inside the x-ray vault, and figure 19 shows the front view of a block.

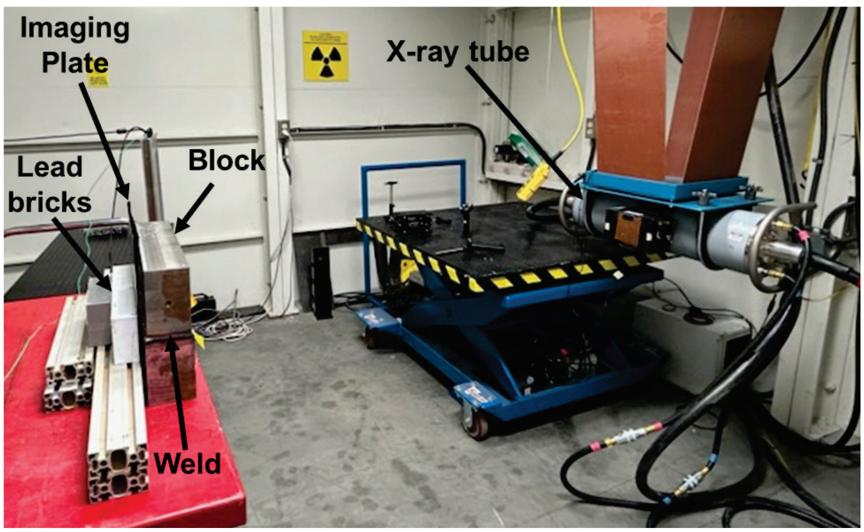


Figure 18: Photograph of the x-ray vault. Lead bricks were placed behind the imaging plate to reduce backscatter.

[1] ImageJ is Java-based image analysis software available for free at https://imagej.nih.gov/ij/.

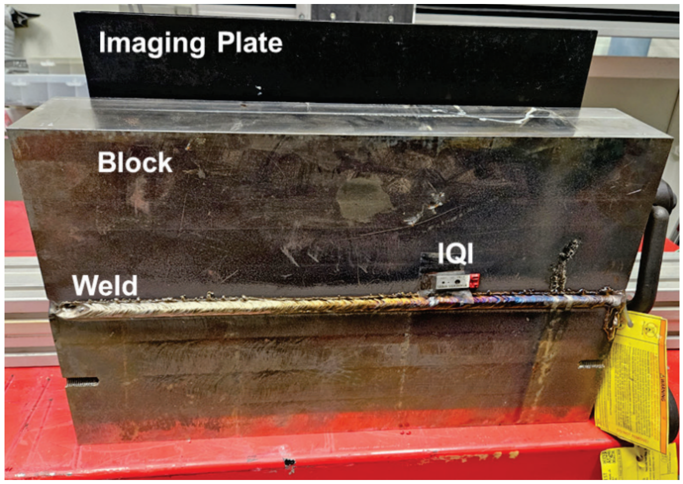


Figure 19: Photograph of a block during radiography. The #50 IQI was placed adjacent to the weld joint.

## 5.2 Ultrasonics

### 5.2.1 FMC

The FMC scans were performed with an Eddyfi Emerald system coupled with a ZMC2 motor controller and an ATCO encoded scanner and motor arm. Line-scan data were collected by translating the probe parallel to the joint line. Data were collected with three different array probes because 1) FMC data can be collected relatively rapidly with line scans, so there was little additional cost to collecting data with multiple probes, and 2) This was our first experience with EBW mockups and would be our only opportunity to examine these blocks, so we chose to be comprehensive. The nominal probe frequencies were 3 MHz, 4 MHz, and 5 MHz. Each probe had a different element layout. The 3 MHz probe elements were arranged in an 11×11 square, the 4 MHz probe was a 32×1 linear array, and the 5 MHz probe was a 32×4 array. The Emerald system had 64 channels, so a subset of the elements was used with the 3 MHz and 5 MHz probes. For the 3 MHz probe, an 11×5 submatrix was used (11 in the primary axis and 5 in the secondary axis). For the 5 MHz probe, a 32×2 submatrix was used. These layouts were chosen because it was more important to have sensitivity in the primary direction—the direction looking toward the weld and into the depth of the component—than in the secondary direction. The probe specifications are shown in table 2. Note that the center frequencies and bandwidths are reported as averages over all the elements. All FMC data were collected using shear waves.

Table 2: FMC Probe Specifications

| Nominal Frequency (MHz) | Center Frequency (MHz) | Element Layout (primary × secondary) | Element Size (primary × secondary) (mm) | Aperture (mm$^2$) | Bandwidth (%) |
|---|---|---|---|---|---|
| 3 | 3.2 | 11×5 | 1.5 × 1.5 | 153.6 | 65 |
| 4 | 3.75 | 32×1 | 0.9 × 8.0 | 255.2 | 84 |
| 5 | 5.0 | 32×2 | 0.38 × 2.46 | 76.6 | 64 |

Data were acquired along the scan axis at 2 mm intervals. Several line scans were collected with each probe at approximately 20 mm intervals from the joint line. Figure 20 shows the top of block 3 as it was being scanned with the 3 MHz probe. The white arrow indicates the probe and the yellow arrow points to putty that was used to dampen reflections within the wedge. The black arrow indicates the direction of motion. Recirculated water from a catch basin below the block was used for ultrasonic coupling (note that the orange appearance is due to rust accumulation over time). Data were reconstructed using the total focusing method (TFM) of delay-multiply-and-sum (DMAS) (ASME 2023; Prowant et al. 2023). Data were visualized and analyzed using UltraVision software.

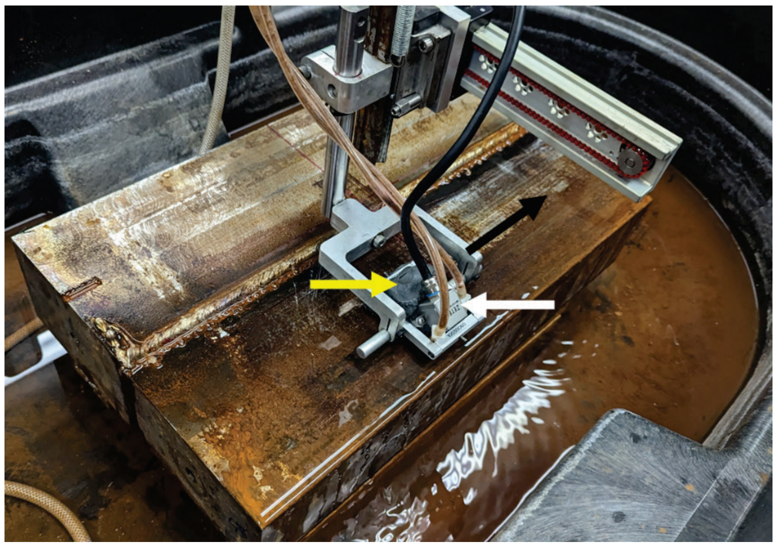

Figure 20: The top of block 3 being scanned with the 3 MHz array probe. The white arrow points to the probe, the yellow arrow points to damping putty, and the black arrow is the scan direction. The block is shown sitting in a water basin; the water was circulated for ultrasonically coupling the probe to the block.

### 5.2.2 0° UT

As described in section 4, 0° UT was used to characterize the weld joints. A 10 MHz, 6.4 mm diameter unfocused probe was used. A Zetec DYNARAY system was coupled with a ZMC2 motor controller and an ATCO encoded scanner and motor arm. The block was supported on one side, and the scan was performed from the opposite side, as shown in figure 21, such that the direction of sound propagation was perpendicular to the weld. The white arrow in the figure is pointing to the probe. Scan resolution, along the width of the block, was 0.5 mm, and index resolution, along the length of the block, was 1 mm. Data were visualized and analyzed using UltraVision software.

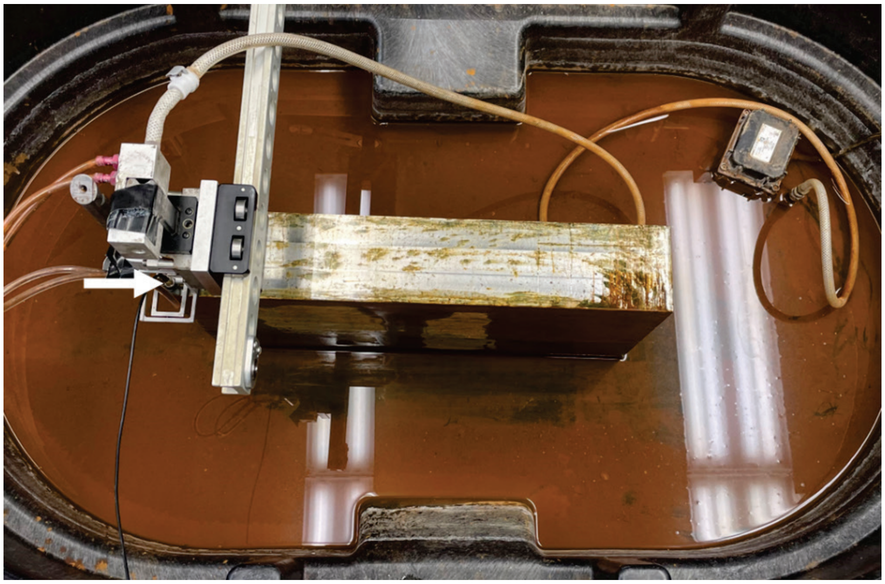

Figure 21: A 0° UT scan being performed on the side of a block. The white arrow is pointing at the probe.

### 5.2.3 TOFD and Tandem

The TOFD and tandem scans were performed with a Zetec DYNARAY system coupled with a ZMC2 motor controller and an ATCO encoded scanner and motor arm. The system was controlled through UltraVision 3 software. The probes were 6.4 mm diameter, single-element 5 MHz probes mounted to 45° shear wedges water-coupled to the blocks with a recirculating pump. Resolution in the scan direction (perpendicular to the weld) was 0.5 mm, and resolution in the index direction (parallel to the weld) was 1 mm.

For TOFD scans, the probes were mounted in a fixture so that they were facing each other and separated by 180 mm. This spacing was determined by the thickness of the blocks and the refraction angle of the probes, which was 45° shear, such that a direct backwall echo would be received. This varied from conventional TOFD, where the probe spacing is somewhat closer. With the required probe spacing, the block was too narrow to scan the entire weld (see section 3.3.2), so the blocks were scanned from both the top and bottom surfaces to achieve full coverage. Figure 22 shows a photograph of block 2 during TOFD scanning.[1] The block is shown sitting in the water basin. The approximate location of the joint line is indicated by the blue line.

[1] Note that this photo was taken during TOFD test scans using different refraction angles and probe separations. The probe separation shown is not the 180 mm used in the final TOFD scans.

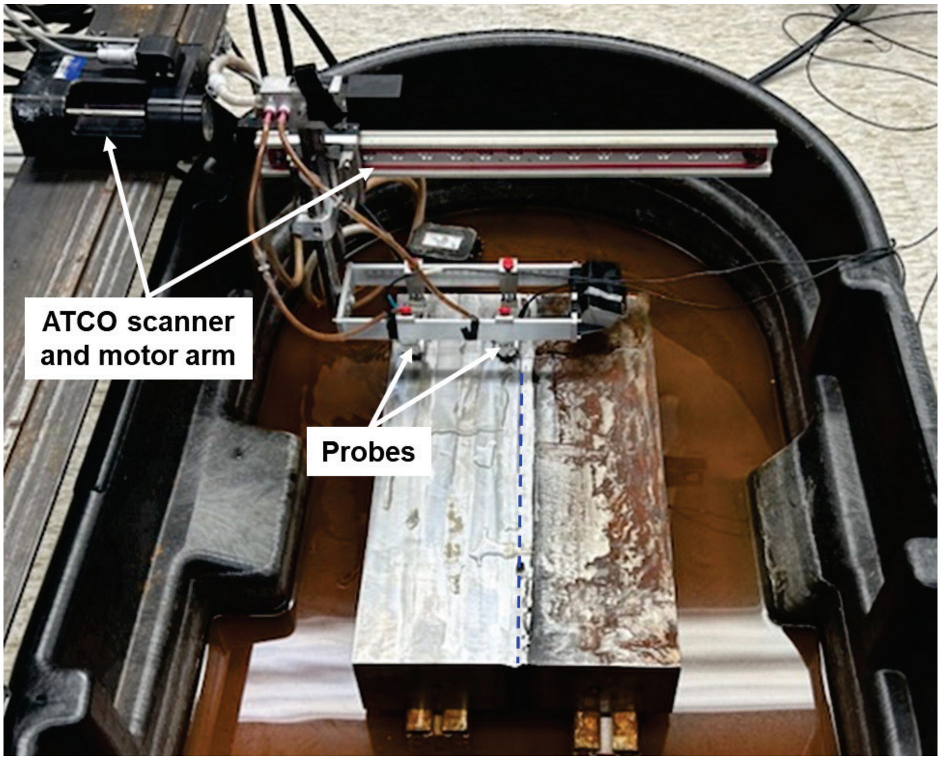


Figure 22: Block 2 during TOFD scanning. The blue line indicates the approximate position of the joint line.

For the tandem scans, the probes were mounted with about 40 mm spacing between them. Due to the length of the wedges, this was nearly as close as the probes could be to one another without touching. The front probe was the transmit probe and the rear probe was the receive probe. As with the TOFD scans, resolution in the scan direction (perpendicular to the weld) was 0.5 mm, and resolution in the index direction (parallel to the weld) was 1 mm. Figure 23 shows a photograph of the top of block 2 during tandem scanning. The blue dashed line indicates the approximate location of the joint line. The white arrow is the transmit probe, and the red arrow is the receive probe. For both TOFD and tandem methods, data were visualized and analyzed using UltraVision software. We tested the rear probe as the transmit probe; however, undesired surface wave signals were picked up by the receive probe. Thus, tandem data were collected with the front probe as the transmit probe.

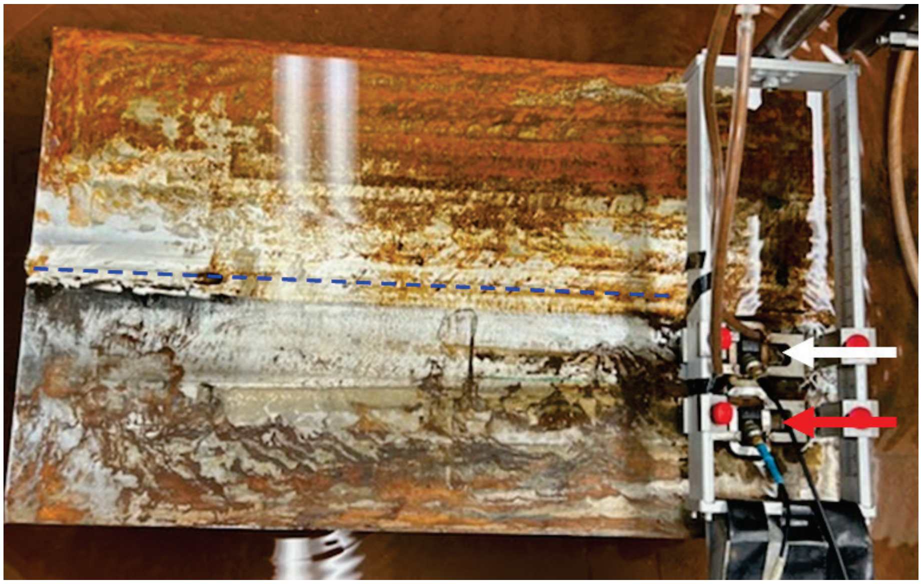

Figure 23: Block 2 during tandem scanning. The white arrow is the transmit probe and the red arrow is the receive probe. The blue line indicates the joint line.

# 6.0 Results and Discussion

## 6.1 Radiography

Overall, the radiography was not helpful in revealing the weld defects. This was not surprising due to the nature of the defects and the thickness of the blocks. The small opening dimension of the LOF and LOP defects did not provide enough of a density variation along the x-ray path to be detectable, even under the ideal condition with the x-ray beam incident exactly parallel to the joint line. Two examples are shown below.

Figure 24 shows a radiograph from block 3, which had substantial LOF along most of the weld joint. A portion of the LOF defect was *potentially* visible as a straight line, but the depth or severity of the LOF was not apparent. The deviation in the weld root was also faintly visible, although it was seen more readily with the eye as in figure 14. The gap between the lead bricks was prominent from x-ray exposure through the back of the imaging plate, showing that x-ray backscatter was significant. The IQI number was barely visible, and none of the IQI holes were visible, nor were the IQI borders.

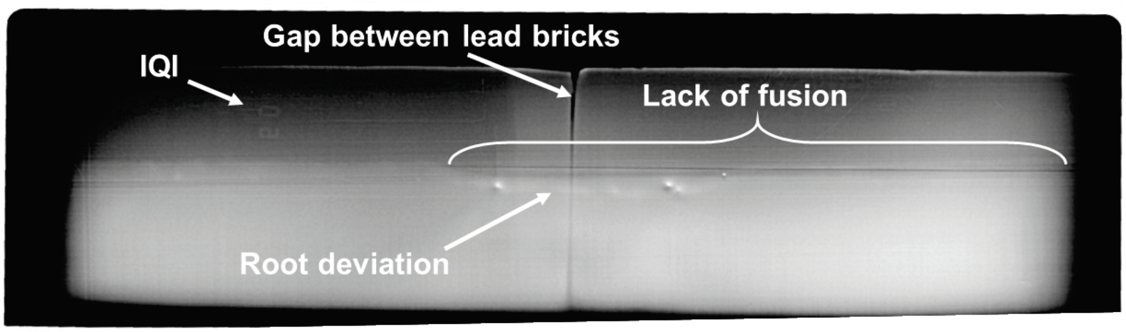


Figure 24: Radiographic image of block 3.

Figure 25 shows an example from block 4, which had an LOP defect along the entire length of the block. The LOP defect was apparent in the image as a straight line that would otherwise be obscured by the weld root. Naturally, a radiograph is not needed to see to lack of weld root, which was readily visible with the eye (see figure 16). The radiograph did not give any information about the depth of the LOP. The flaw opening dimension was too small to be visible, and radiographs taken at an angle to try to show the LOP depth would simply increase the metal path of the x-rays, further reducing exposure.

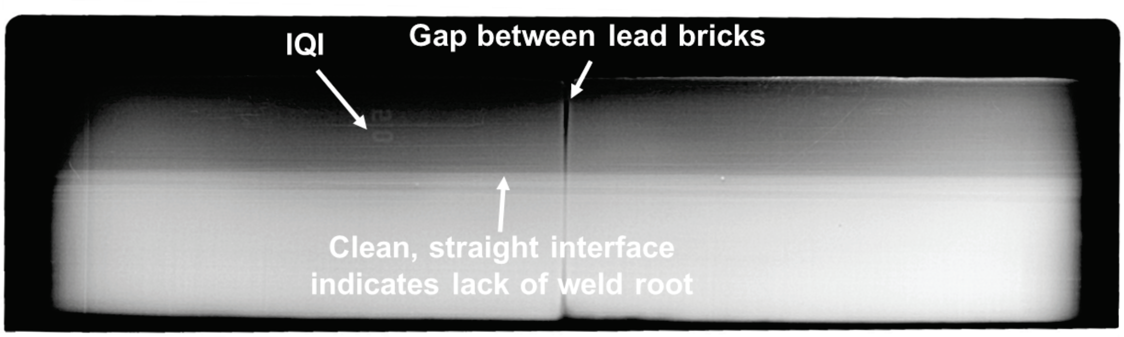


Figure 25: Radiographic image of block 4.

Radiographs from the other mockups are not shown herein because the radiography was generally not helpful for identifying flaws in the weld joints that were not otherwise visible. We note that the keyhole defect in block 2 was readily visible in the radiographs, but it was also visible by eye. Due to the thickness of the mockups, there was insufficient image contrast to see the 2T hole of the IQI or to see the outline of the IQI (which are required for radiographs), and the lead IQI number was barely visible. The strong backscatter, even with the lead brick backing, caused additional exposure to the imaging plate and further reduced image contrast. Even with the x-ray beam centerline aligned with the weld joint, the lack of fusion flaws were not readily visible because the block surfaces were machined smooth and fit tightly together. Based on these results, we do not recommend radiography for inspecting electron beam welds for LOP or LOF defects in thick-walled metal components.

## 6.2 Ultrasonics

### 6.2.1 FMC Results

Three different probes were used to collect the FMC data resulting in a large volume of data for analysis. To streamline the data analysis, we first reviewed the data collected with all three probes on block 2. We qualitatively evaluated the noise levels, the presence and sharpness of weld root signals, the appearance and detectability of weld defects, and the impact of wedge artifacts and other artifacts.

Figure 26 shows example scans (top, end, and side views) with the different probes. The front of the wedge was either 40 mm or 45 mm back from the joint line, as noted, and data were acquired from the top surface of the block. The LOF and keyhole defects are indicated in addition to the weld root response. Echoes within the wedge can present as artifacts; examples of these are pointed out as well. Wedge echoes can be identified by their curved shape in the side views and by their presence along the entire scan line in the top or end views. Wedge echoes can also identified because they can be damped by application of damping material, such as putty (cf. figure 20) or pressing with a finger. Note that the color scale shown in figure 26 applies to all figures in this subsection.

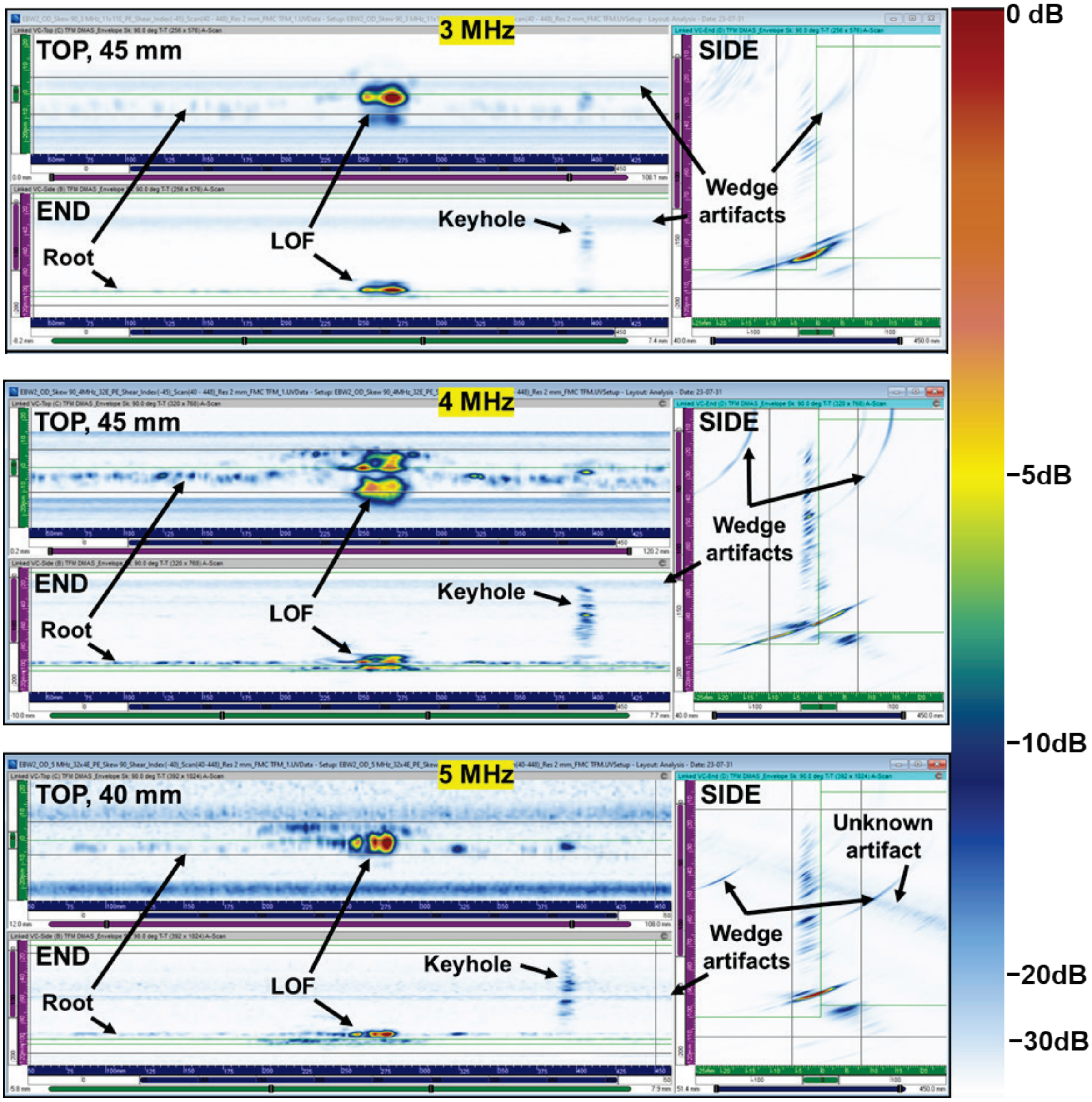


Figure 26: Example FMC scans of block 2 with the three different probes.

In the 3 MHz scan, the LOF defect was prominent, but the root and keyhole echoes were only faintly visible. Wedge artifacts were present but not obtrusive. The 4 MHz scan clearly showed the LOF defect, and the root and keyhole echoes were stronger and easily identifiable. The wedge artifacts were also stronger, but they mostly occurred outside the regions of interest and therefore did not interfere with data interpretation. The echoes in the 4 MHz scan appeared to be considerably "sharper" or better focused than those in the 3 MHz scan. The 5 MHz scan clearly shows the LOF and keyhole echoes, but the root echo was relatively weak. The echoes did not appear to be as sharp as those in the 4 MHz scan. The wedge artifacts were not obtrusive, but an additional unknown artifact was present in the 5 MHz scan. In the side view, this artifact permeated diagonally through the joint line resulting in the top and end views appearing to have noisy backgrounds. Overall, we judged that the 4 MHz probe provided the best results, so we focused on evaluating the 4 MHz scans for the remainder of this section.

The 4 MHz probe had the largest aperture and bandwidth (see table 2), so it is not surprising that it appeared perform better than the other two probes. A study of FMC probe performance is beyond the scope of this work, but it is worth noting that differences in the image quality, such as noise levels, resolution, and echo amplitudes, are a result of the different element sizes and array layouts. Some variations in echo response characteristics are also expected due the different probe frequencies.

A couple of empirical factors had an effect on the FMC scans. First, recall that one side of the block was 90 mm thick and the other 100 mm thick (the scans in figure 26 were acquired from the 100 mm thick side of the block). Some subtle variations in backwall responses or corner echoes due the thicknesses difference were visible depending on which side of the weld the data were acquired from. However, all other features, particularly the flaw responses, were substantially the same from either side of the weld. Second, data were acquired from various distances from the joint line. Probe positions closest to the joint line led to better visualization of the upper portions of the weld while positions further back better showed the bottom portions. For brevity, herein we present only the scans that best show the weld and defect characteristics that are being discussed.

Figure 27 shows the 4 MHz scan of block 1 (ideal weld conditions) at 45 mm back from the joint line. There are no indications of note in the scan other than the weld root. The weld region is visible in the side view as a vertical column of signal slightly above the noise background; this signal is attributed to backscatter from the weld microstructure. Some scatter is also visible throughout the end view as light blue speckles.

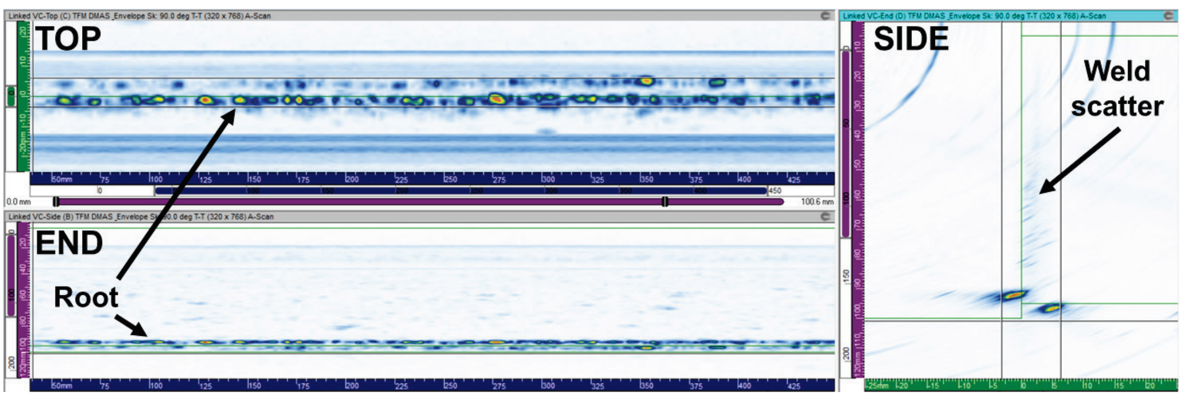


Figure 27: FMC scan of block 1 from the top surface.

Figure 28 shows the 4 MHz scan of block 2 (small LOF and through-wall keyhole) at 45 mm from the joint line. The LOF defect is clearly visible, although it is unclear if it can be accurately depth-sized. The strong echo is from the corner of the unfused portion and indicates that the LOF is surface-connected; this echo is not necessarily a specular reflection from the defect itself. Recall the face of the defect is smooth and vertical, so we do not expect an appreciable specular echo using a PE method. No tip signals were detected. The keyhole defect is also clearly visible. The echoes from the keyhole are strongest through approximately the midpoint of the specimen due to the position of the probe. We observed that scans closer to the joint line better insonified the top portion of the keyhole while scans further back better insonified the bottom portion. In the side view, the weld scatter observed in figure 27 is obscured by the stronger echoes from the keyhole, although some low-amplitude scatter was visible in the end view as light blue speckles.

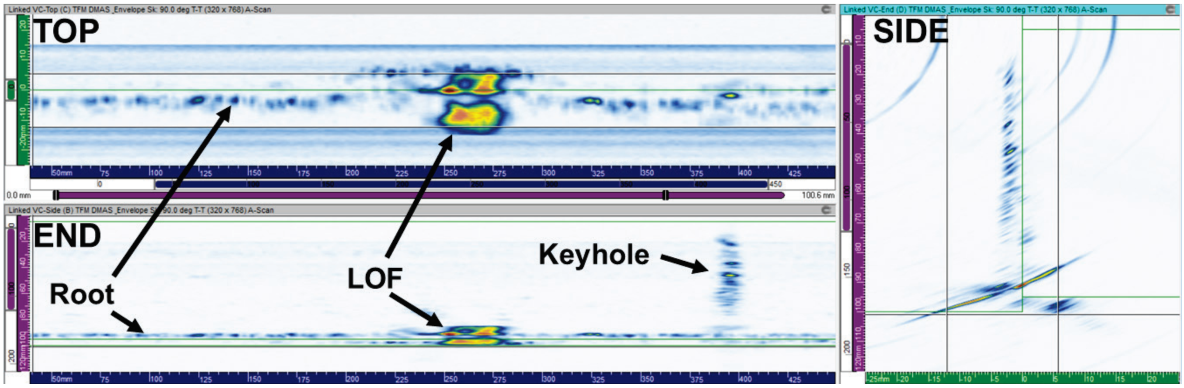


Figure 28: FMC scan of block 2 from the top surface.

Figure 29 shows two scans of block 3 (large LOF) at 20 mm and 45 mm from the joint line. There is a prominent corner echo except where the block was fused. The fusion zone is indicated by the black bracket. The hourglass shape of the fusion zone, as shown in figure 15, is faintly visible in the end views from scatter-like signals highlighted by the red dotted lines in the 20 mm scan. Note that the soft gain was turned up high enough to see those faint signals, which resulted in the corner echo signal being strongly saturated. Echoes from the fusion line near the top surface are visible in the 20 mm scan (and appear more faintly in the 45 mm scan). We hypothesize that the top portion of the joint line was fused because visual observation suggested the weld crown was fused to both blocks (see figure 14). Also, the flared shape of the top of the weld zone would be able to fuse the top of the blocks without affecting most of the rest of the joint line, such as illustrated in figure 3 panel B. Other than the fusion-line echo, there were no indications from the FMC scans about the depth of the LOF. For example, looking at the end view, the signal from within the fusion zone (between the red lines) looks identical to the signal from the rest of the block. As described in section 3.3.1, when using PE UT there is no specular reflection detected from the unfused regions because the smooth vertical, planar surfaces of the joint lines reflect sound away from the probe while fused regions are not detected because the sound is transmitted through.

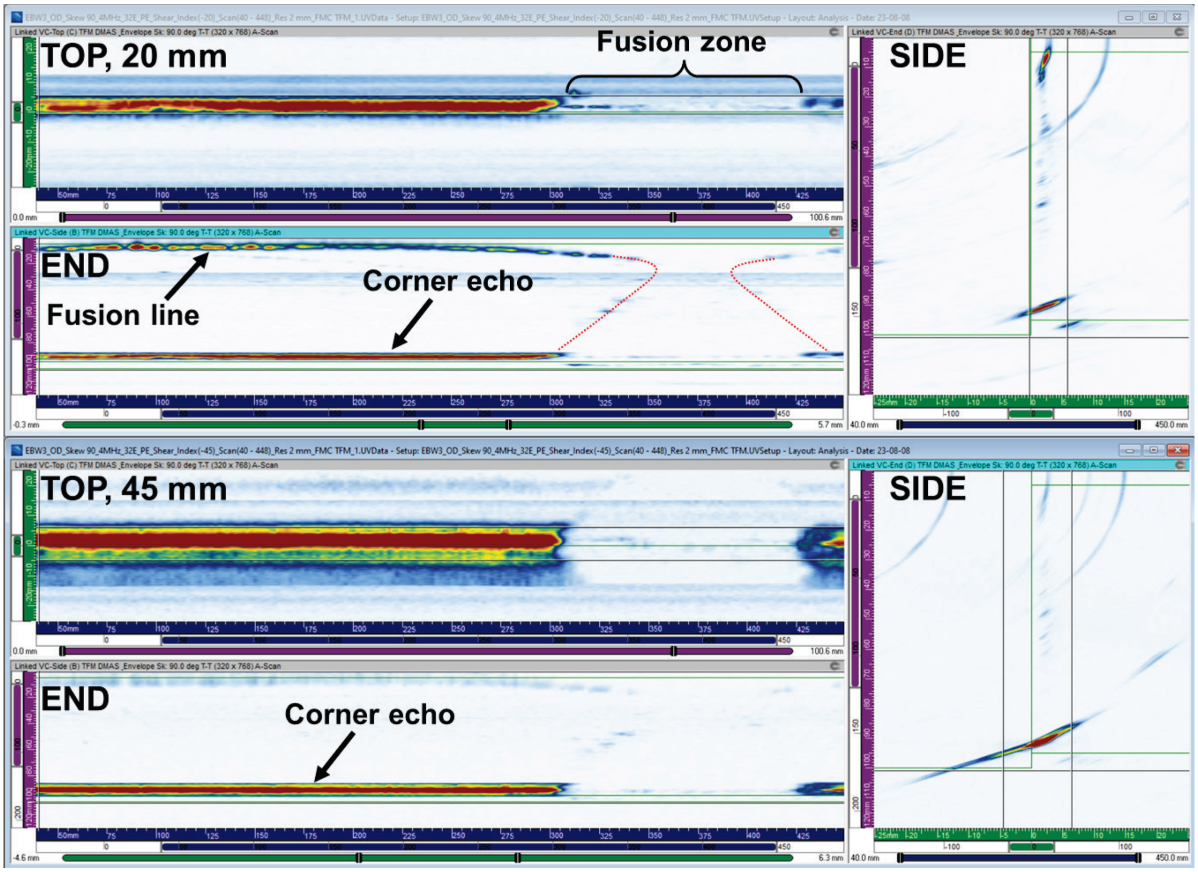


Figure 29: FMC scans of block 3 from the top surface.

Scans from the bottom surface of block 3 are shown in figure 30. In this case, the fusion line appeared at the bottom of the 45 mm scan (much more faintly in the 20 mm scan) and could potentially be misconstrued as a crown signal. There was no corner echo to delineate the fusion zone since the top of the weld appeared to be fused along the entire block. Echoes from the boundary between the fused and unfused areas (red dotted lines in the 20 mm scan) were readily visible, and we interpreted them as weld defects. However, based on our experience with conventional V welds, there was not compelling evidence of a substantial LOF defect in this image.

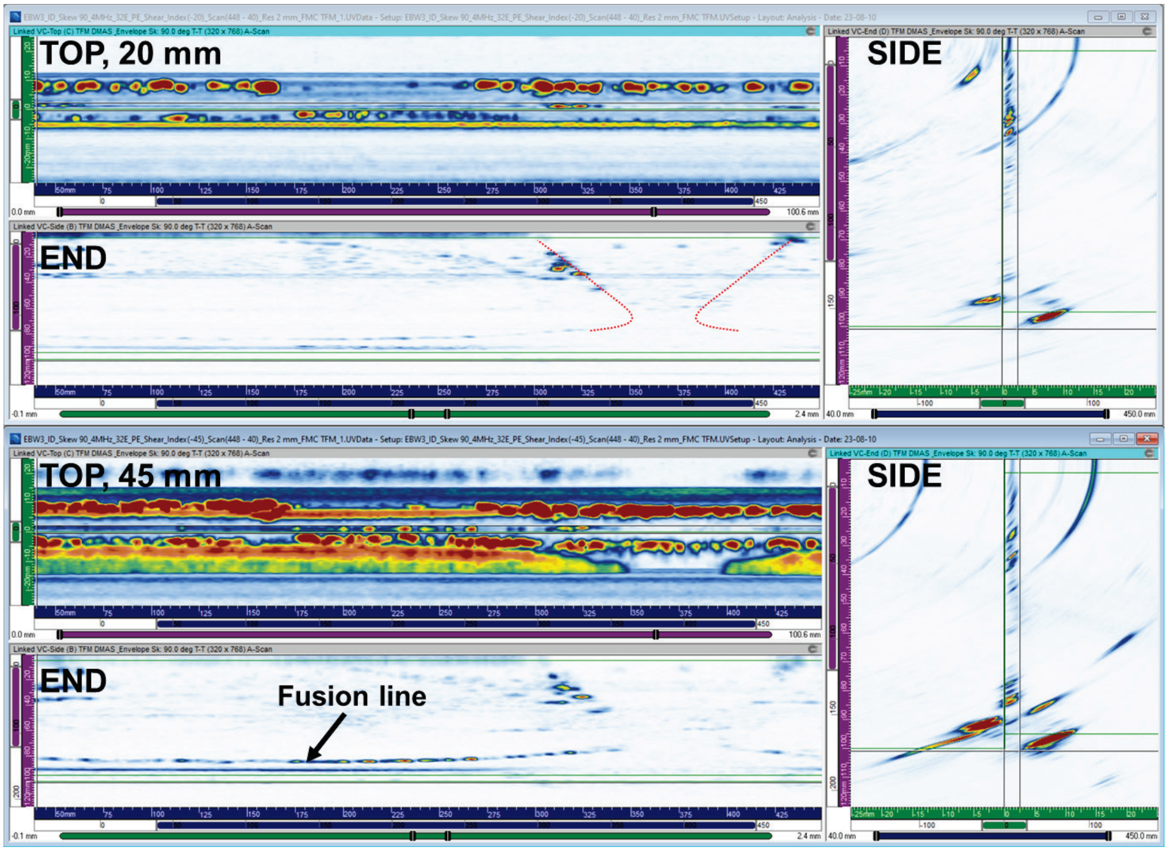


Figure 30: FMC scans of block 3 from the bottom surface.

The FMC scan of block 4 (LOP along the full length) at 45 mm from the joint line is shown in figure 31. As with the scans from block 3, the soft gain was increased such that the corner echo was strongly saturated so other features would be visible. The presence of a corner echo across the entire scan suggested that there was an LOP defect. However, because it does span the entire block, the corner echo could easily be mistaken for a root echo in a blind test. The depth of the LOP was only faintly visible in the side view with the gain turned up high and measured to be about 5 mm. We recognized the LOP signal because we knew from the 0° scans that the LOP depth was likely less than 10 mm (see section 4.5). The LOP echo was not any more prominent in scans at different distances from the joint line, and it was not visible at all in the scans from the bottom surface. The rest of the scan appeared similar to that of block 1.

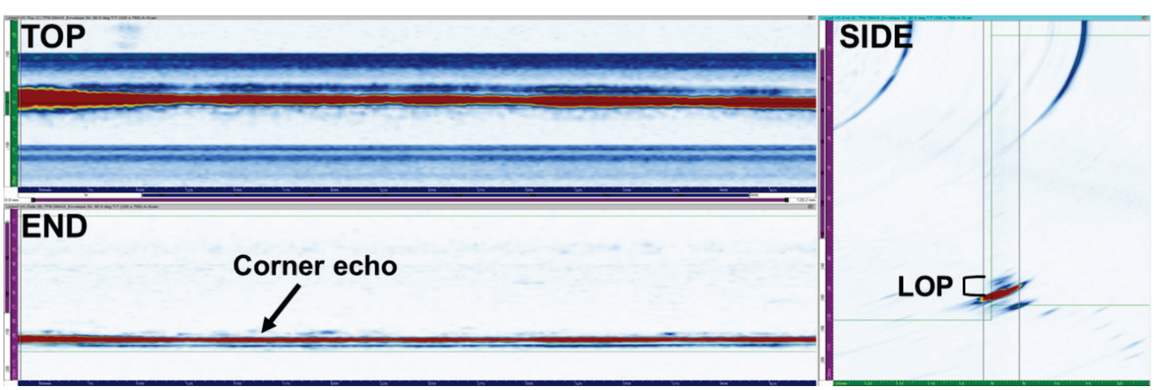


Figure 31: FMC scan of block 4 from the top surface.

Overall, the FMC data showed strong corner echoes where corners were not fused, weld root echoes where corners were fused, weld crown echoes, and indications of LOF and LOP defects. However, results confirmed the problem illustrated in figure 4, where depth sizing of the LOF defects was challenging due to lack of specular echoes from the joint line. Based on the results shown in this section, we do not recommend PE approaches for inspection of simple square electron-beam butt welds.

We note the lack of tip diffracted signals observed in the FMC scans even though 4 MHz shear waves should be well-suited for detecting such signals. Blocks 1 and 3 did not have defects with tips. Block 4 had a shallow LOP, and the tip response from that would have been lost in the corner echo signal. Block 2 had a LOF defect that may be expected to return a tip signal. We do not know exactly why a tip signal was not observed on that block, but there are a few points to consider. First, tip diffracted signals emanate from sharp corners, such as crack tips and notch corners. The exact morphology of the LOF defect is not clear; it is neither a crack nor a notch, and it may lack the attributes required to radiate a strong tip diffracted signal. Second, probe elements are fired individually, so the beam spread of each transmitting element must be considered, not the entire probe aperture. Small elements, such as those in the array probes, have large angular beam spread and therefore large effective spot sizes and poor penetration. Third, the plates were thick, which exasperates the element size issue by creating long metal paths. Fourth, a tip signal may have been present but poorly resolved from the rest of the defect signal.

### 6.2.2 TOFD Results

TOFD scans were acquired from both the top and bottom surfaces of the blocks so that the entire thickness of the blocks could be covered, since the blocks were not wide enough to accommodate a full scan due to the required probe separation. Figure 6 illustrates the coverage and relative probe positions. In this section, scans from the top and bottom surfaces are shown together. The vertical axes represent the depth into the block, where the negative portion of the axis is a reflection of the positive axis (the symmetry of this axis is described in section 3.3.2.) The horizontal axis is the position along the length of the weld.

The TOFD scans of block 1 (ideal weld parameters) are shown in figure 32. The top and bottom panels are the scans from the top and bottom surfaces, respectively. The joint line is indicated by the white horizontal lines. Overall, the signal strength was relatively high (red is the strongest signal; see the logarithmic color scale on the right) indicating that there was little in the weld region to interfere with the sound energy transmission. Recall that strong signals in the TOFD scans indicate the sound energy was not impeded in its path from the transmit probe to the receive probe. Some variations in the signal strength were likely due to surface conditions and probe coupling. In the bottom scan, some horizontal bands of signal variation were observed flanking the joint line, as indicated by the black brackets. We hypothesize that these regions were due to scattering effects from the tapering at the top of the weld (see figure 2).

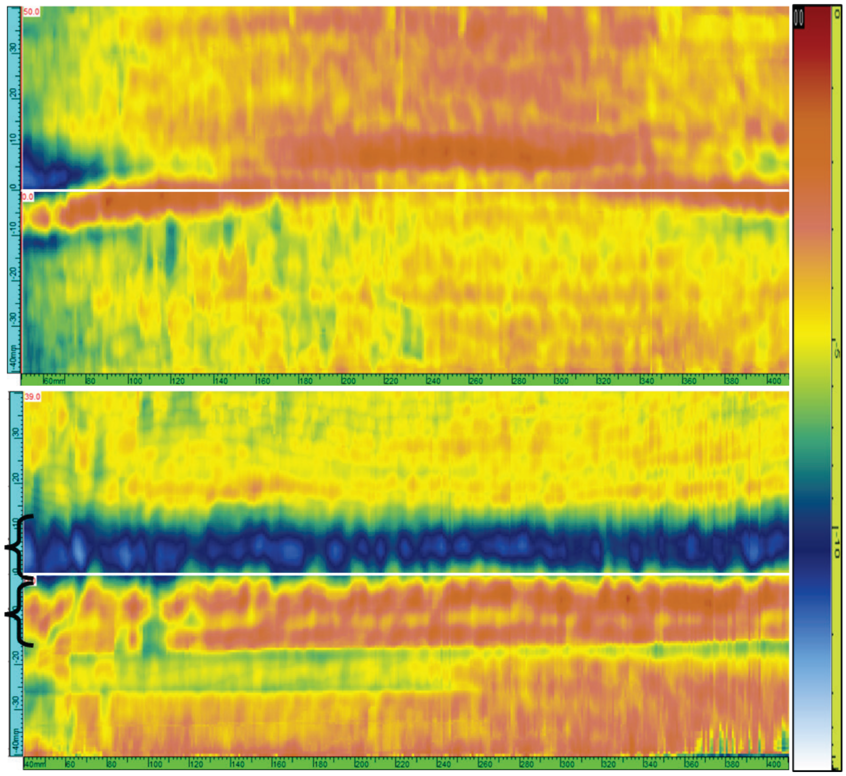

Figure 32: TOFD scans of block 1. Top: scan from the top of the block. Bottom: scan from the bottom of the block. The color scale indicates signal intensity with red being the highest.

Figure 33 shows the TOFD scans of block 2 (small LOF and through-wall keyhole). The top and bottom panels are the scans from the top and bottom surfaces, respectively, and the joint line is indicated by the white horizontal lines. As with block 1, there is relatively strong and uniform signal intensity throughout, except for the unfused region and the keyhole. These defects blocked the sound energy from reaching the receive probe, so they appeared with low signal intensity. Unlike in the FMC scans, the TOFD images allowed for depth sizing. We measured the depth of the LOF to be approximately 25-30 mm, which was consistent with the measurement from the 0° scan. Bands of weak and strong signal were visible in the bottom scan, as with block 1. Similar signal variations were visible in the top scan, but we could not identify their cause. Recall the weld crown and root were machined smooth prior to acquiring these images, so the signal variations in the top scan were not due to a protruding weld root.

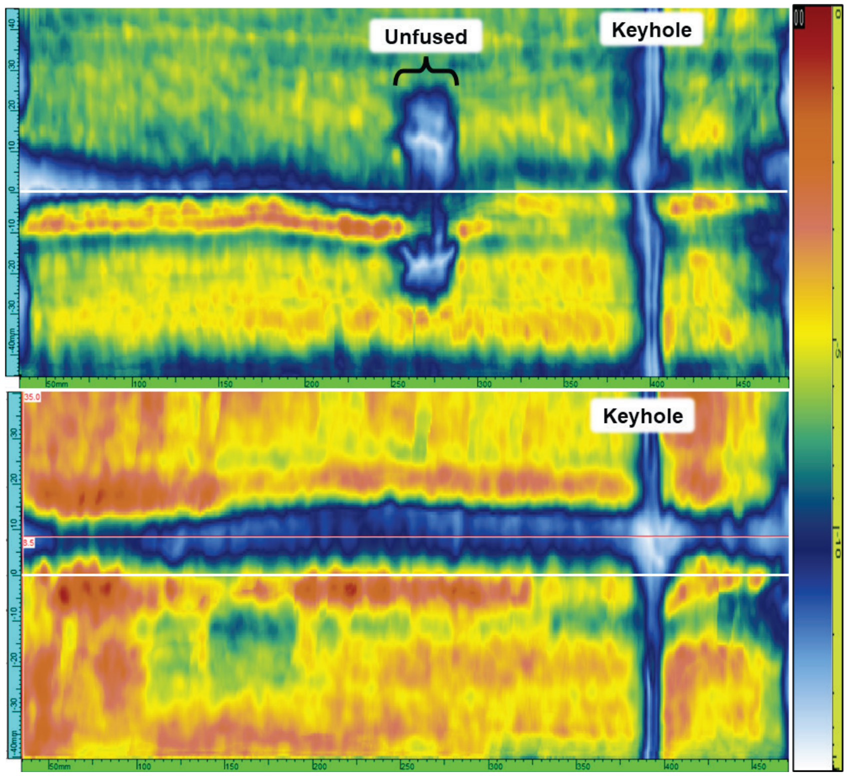


Figure 33: TOFD scans of block 2. Top: scan from the top of the block. Bottom: scan from the bottom of the block. The LOF and keyhole defects are labeled. The color scale indicates signal intensity with red being the highest.

Figure 34 shows the TOFD scans of block 3 (large LOF). The top and bottom panels are the scans from the top and bottom surfaces, respectively, and the joint line is indicated by the white horizontal lines. The large LOF area was evident by the lack of signal throughout most of the scans. In the top scan, the bottom portion of the LOF is visible, and vice versa. Together they form the hourglass shape observed in the 0° scan (see figure 15). A band of high signal intensity was visible in the bottom scan, likely indicating that the top of the weld was at least somewhat fused. As discussed above, the FMC scans in figures 29 and 30 also suggest some fusion at the top of the joint line. Again, the weld crown was machined smooth prior to these scans, so the signal band in the bottom scan was not due to the weld crown.

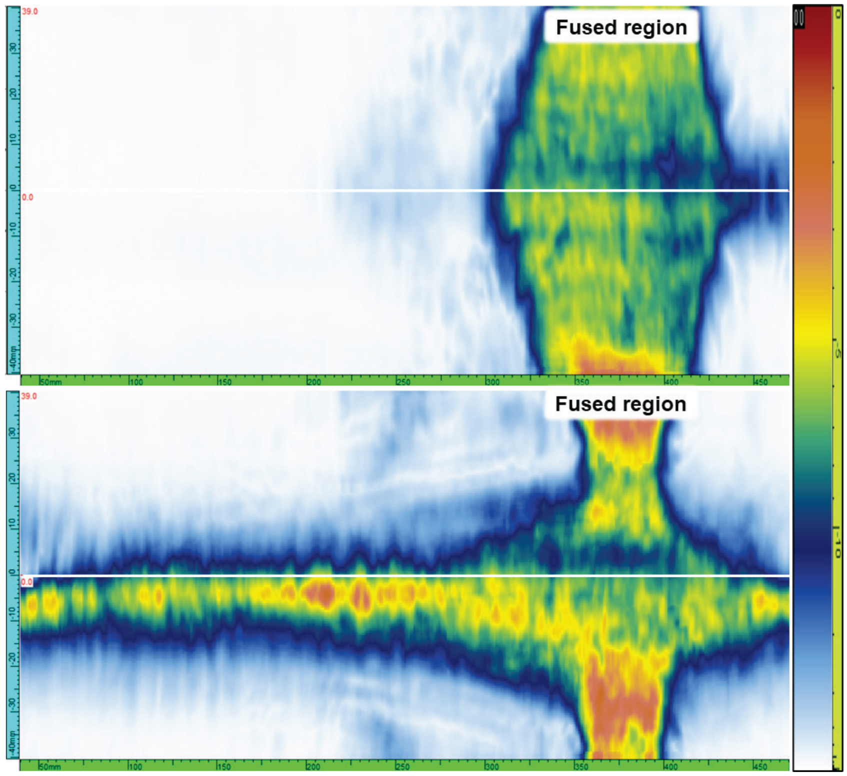


Figure 34: TOFD scans of block 3. Top: scan from the top of the block. Bottom: scan from the bottom of the block. The regions where fusion occurred are labeled. The color scale indicates signal intensity with red being the highest.

The TOFD scans of block 4 (LOP along the full length) are shown in figure 35. As with block 1, there was relatively strong and uniform signal throughout, indicating a fused weld joint. The banding in the bottom scan that was visible in the block 1 and block 2 scans was also visible in the block 4 scan. The LOP defect in block 4 was visible in the top scan as a band of lower signal intensity, indicated by the black bracket. The width of the LOF band was measured at approximately 11 mm at the −6 dB drop in signal intensity, which means the LOP defect was about 5.5 mm deep (recall from section 3.3.2 that a TOFD scan with this setup is symmetric about the joint line). The LOF depth agreed with that from the FMC measurement, but the defect was readily apparent with TOFD whereas it was difficult to identify with FMC.

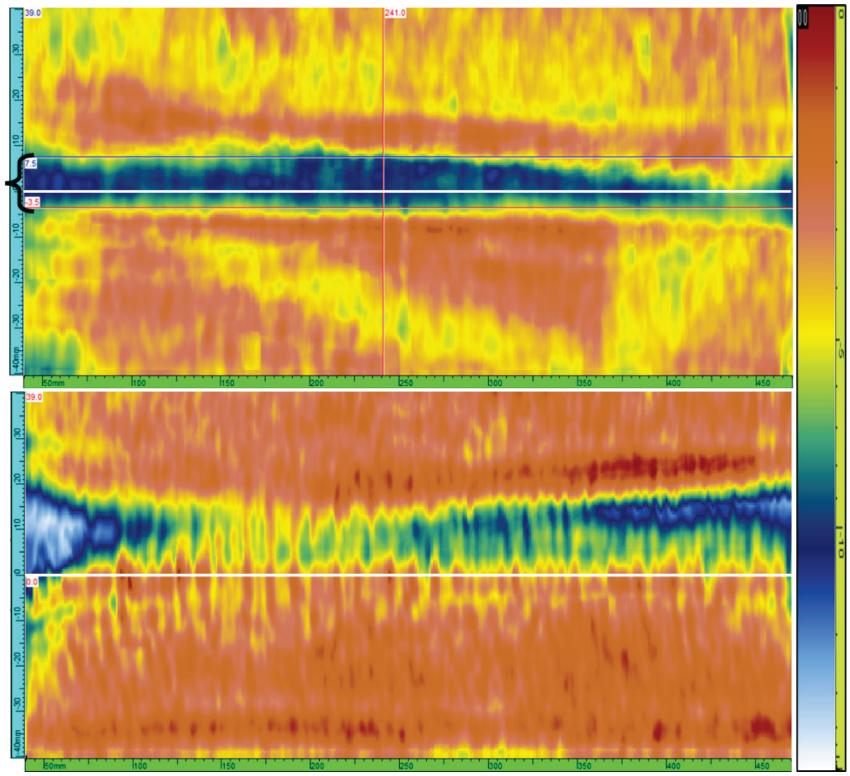

Figure 35: TOFD scans of block 4. Top: scan from the top of the block. Bottom: scan from the bottom of the block. The LOP defect is indicated in the top scan by the black bracket. The color scale indicates signal intensity with red being the highest.

Overall, the pitch-catch TOFD setup was effective at helping identify and size the weld defects. We note that the UT signals observed using our TOFD setup are different from those typically observed when using a conventional TOFD approach, where tip diffracted signals are of primary interest. Figure 36 is an example of diffracted tip signals (white arrows) from a conventional TOFD scan (Cumblidge et al. 2010). Our TOFD signals were also different from those from typical PE approaches, where a defect causes an echo signal as opposed to a lack of signal, as in our TOFD approach. Therefore, we suggest that additional training will be needed to familiarize inspectors with how to recognize and interpret the types of signal responses that this TOFD method will give when inspecting EBW joints similar to those presented herein.

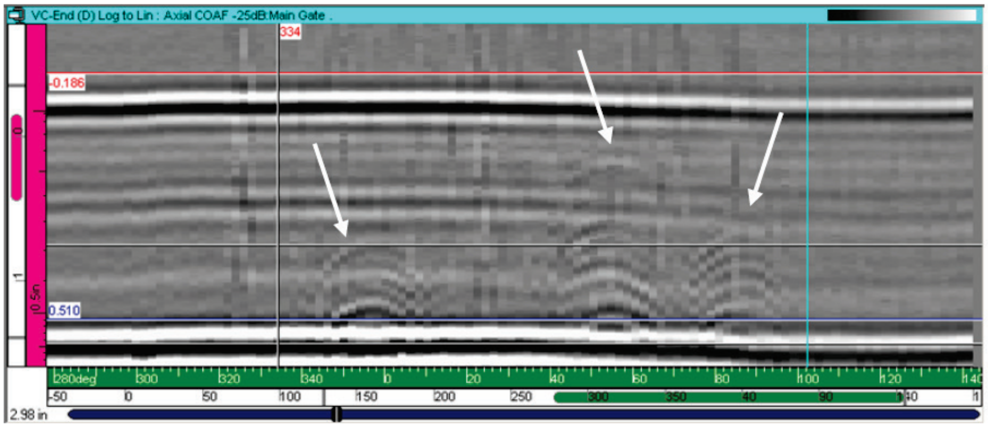


Figure 36: Example of conventional TOFD data. Tip diffracted signals are indicated by the white arrows.

### 6.2.3 Tandem

Figure 37 shows tandem scans from all four blocks. The scans were all acquired from the top surface of the block with the same hardware gain. Different software gains were used in the figure, as noted. The vertical axes are the ultrasound, or depth, dimensions and the horizontal axes are along the length of the welds. The color scale is the same as shown in figure 26.

The scan from block 1 showed what appeared to be a weak weld root signal, but it was recorded in the image at a depth of ≈40 mm. However, recall that the receive probe was about 40 mm behind the transmit probe, so this echo is indeed likely from the joint line at the block's bottom surface. We note that these scans were acquired after the plates were machined smooth, so there was no protruding weld crown or root. Thus, it is unclear exactly what the source of the echo response was. Regardless, it was a very weak response. There was also an artifact from an unidentified source, possibly a wedge echo. The block 2 scan clearly showed the unfused region and the keyhole (again at ≈40 mm depth), but no depth sizing information was available. A root signal was faintly visible at the reduced gain. The block 3 scan showed a strong corner echo (at ≈40 mm depth) with distinct signal intensity differences between the fused and unfused regions; again, no depth sizing information was available despite having scanned across the joint line. Finally, the block 4 scan showed a faint root signal (at ≈40 mm). In this case the root signal was weaker than that from block 1 despite the LOF defect; thus, we do not attribute the root signal to the LOF. The LOF defect was not visible in the tandem scan.

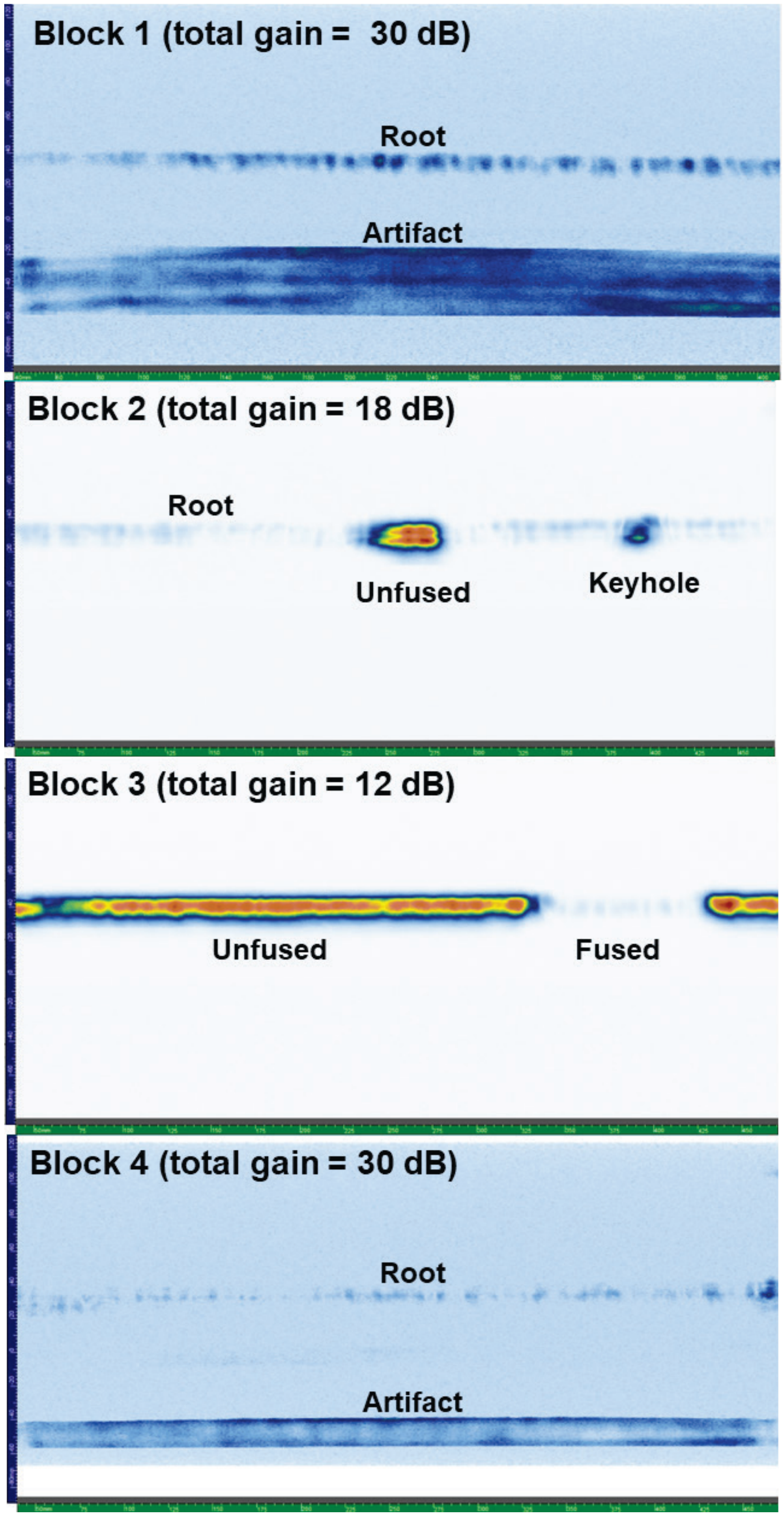


Figure 37: Tandem scans from the top surface.

## 6.3 Heat Treatment

As mentioned in section 3.1, heat treatment can be used to homogenize the grain structure and minimize, or potentially eliminate, any impacts of the weld on UT examinations (Gandy and Stover 2018). Prior to returning the blocks to EPRI, a ~5 cm wide section was cut off block 1 for heat treatment and metallurgical testing.

Prior to heat treatment, we performed 0° UT with 10 MHz longitudinal waves from the top surface of the section at three locations: the joint line, adjacent to the weld (approximately 7 mm from the joint line), and away from the weld (approximately 40 mm from the joint line through parent material). Each measurement was repeated five times. We also performed FMC UT with 10 MHz shear waves from the top surface with sound directed obliquely toward the weld. A Sonatest Veo3 was used. The FMC probe was a 16-element linear array mounted on a 60° shear wedge, had a 5 mm × 5 mm aperture, and was operated in direct (TT) mode.

The heat treatment was performed in three steps as provided by EPRI:

1. solution anneal at 2050°F (1120°C) for 2 hours, then water quench
2. harden at 1650°F (900°C) for 10 hours, then water quench
3. temper at 1200°F (650°C) for 10 hours, then air-cool.

The heat treatment caused significant oxidation to the surface of the cut section. Figure 38 shows the cut face of the section after heat treatment followed by cleaning with an angle grinder wire brush attachment. To perform the post-heat-treatment UT, we had to machine the surfaces smooth, which entailed removing 1-2 mm of material from all faces of the section. Removing that material did not compromise the pre- and post-heat-treatment UT comparisons.

Figure 38: Photograph of the cut face of the section after heat treatment.

Figure 39 shows the polished and chemically etched cut surface before and after heat treatment. Prior to heat treatment, the HAZ and the melt zone were readily visible and were separated by regions of larger and predominantly horizontal grain structure. After heat treatment, the microstructure in the weld was largely homogenized with a faint indication of the joint line and melt zone. The flared region of the top of the weld was visible only under favorable lighting conditions. The grain structure of the parent material also appears to be different, with the grains in the post-heat-treatment photo characterized by a fine speckle appearance.

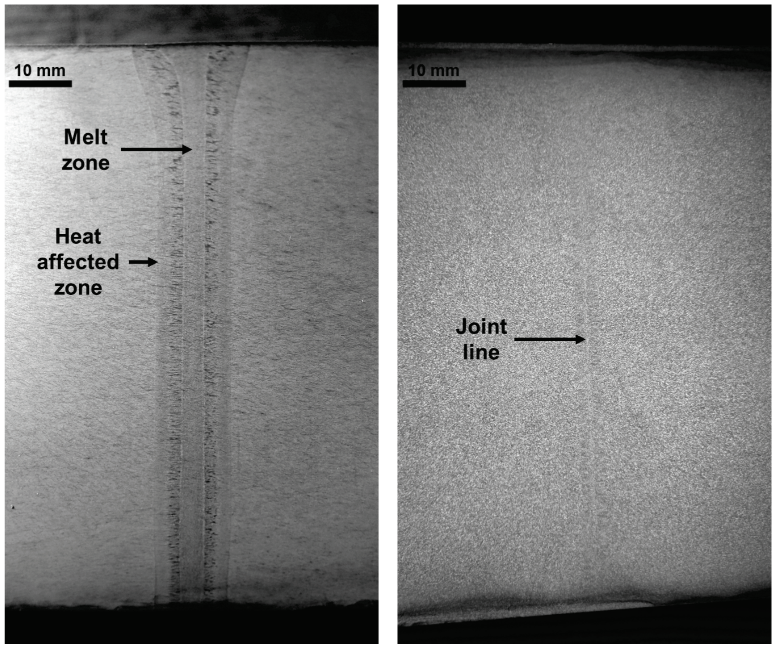


Figure 39: Photographs of the weld region before (left) and after (right) heat treatment.

After heat treatment and machining, we repeated the pre-heat-treatment UT measurements. Figure 40 shows representative A-scans from each position before (left) and after (right) heat treatment. Most A-scans showed typical echo trains, with echo heights reduced in time due to attenuation. However, the pre-heat-treatment A-scan acquired on the joint line (bottom left panel) had second echoes (blue arrow) with higher amplitudes than the first echoes (red arrow). We do not have an explanation for this phenomenon, but it was consistently observed in all five measurements. The post-heat-treatment A-scan (bottom right panel) was more similar to the other A-scans in the figure, confirming that the microstructural changes shown in figure 39 improved the overall inspectability of the weld.

Figure 40 also shows the hardware gains for each scan. Away from the weld (top row), 5 dB (1.78x) less gain was needed for the post-heat-treatment scan compared to pre-heat-treatment scan. Adjacent to the weld (middle row), 10 dB (3.16x) less gain was needed. On the weld (bottom row), 11 dB (3.55x) less gain was needed. The reduced post-heat-treatment hardware gains are a direct indication that the UT properties of the section were improved by changes in the microstructure due to the heat treatment, especially on the weld.

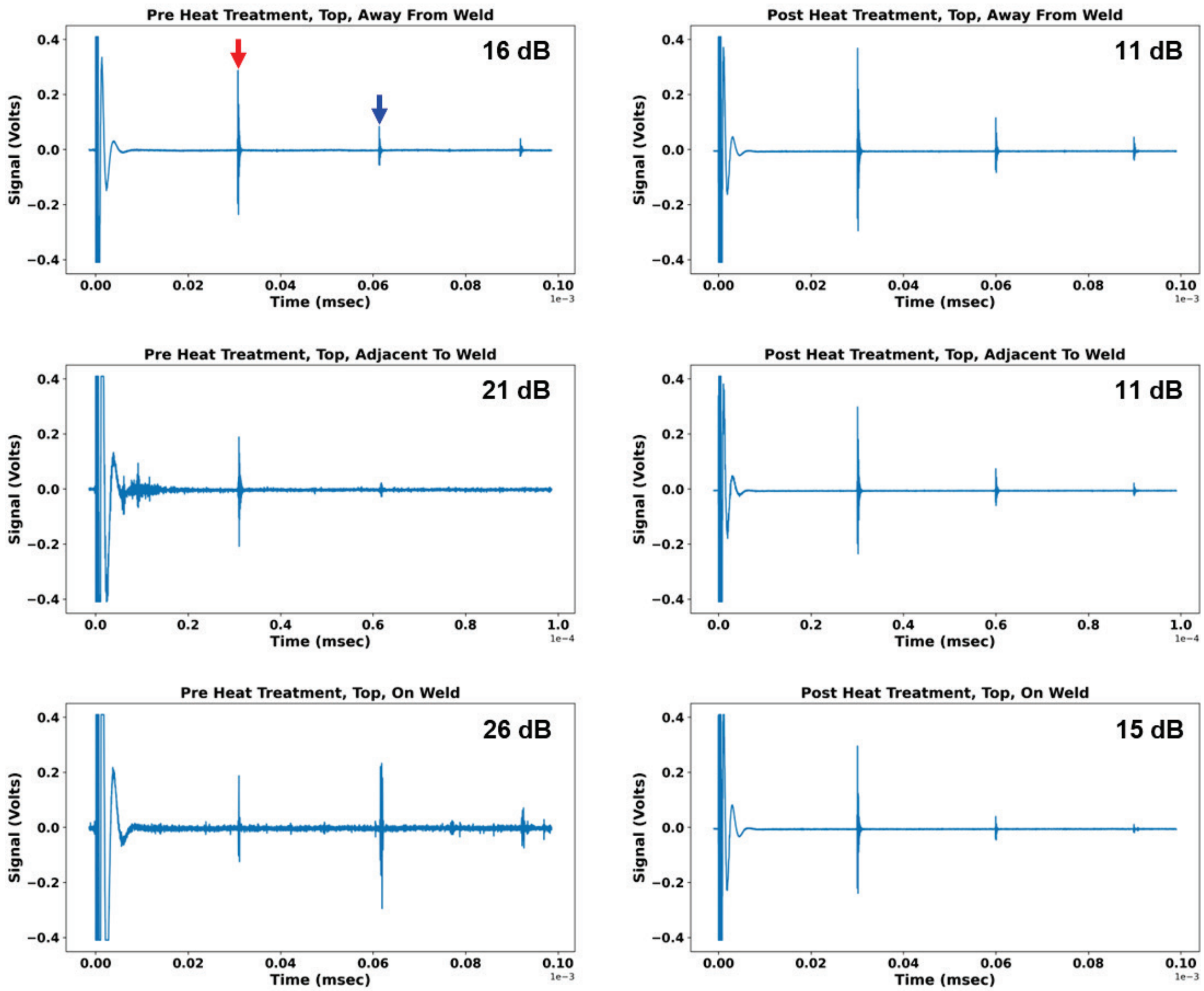


Figure 40: A-scans acquired from the top of the section taken pre (left) and post (right) heat treatment. The red and blue arrows indicate the first and second echoes used to calculate attenuation.

Attenuation values were calculated based on the peak signals of the first two echoes (indicated by the red and blue arrows) using the following formula:

$$A(\mathrm{dB}) = 20\log_{10}\frac{I_2}{I_1} \quad (1)$$

where $A$ is the attenuation in dB, $I_1$ is the first echo amplitude, and $I_2$ is the second echo amplitude. Figure 41 is a bar chart showing the average attenuation values for each measurement set. Prior to heat treatment, there was about 7 dB (2.24x) more attenuation adjacent to the weld than away from the weld (i.e., over parent material). After heat treatment, the difference was only 1 dB (1.12x). On the weld, there was about 4 dB (1.58x) more attenuation after heat treatment than there was through parent material. This can be attributed to the slight difference in microstructure that persisted at the joint line (see figure 39). Note that the pre-heat-treatment attenuation on the weld was not calculated due to the unusual nature of the A-scan, as described above.

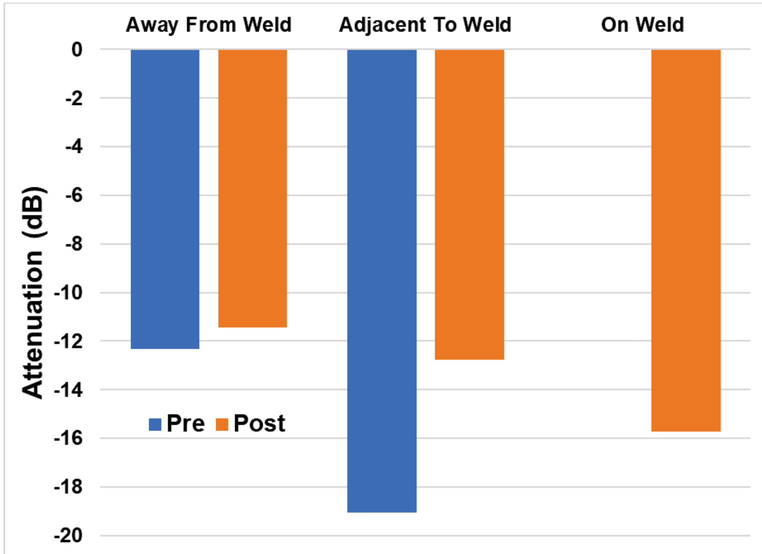


Figure 41: Attenuation values measured pre and post heat treatment.

Figure 42 shows side views of the FMC scans taken before and after heat treatment. The scans show the echo signals; there are no flaws in this region, so all the echoes are due to scatter from the microstructure. Note that the high angle of refraction of the wedge kept the sound field near the top of the section, as illustrated in the figure. The same hardware and software settings were used for both scans. The before scan showed darker regions that appeared to be outlines of the weld, indicated by the yellow arrows. These outlines appeared to follow the same shape as the weld taper that was observed visually near the weld crown. Between the outlines was a region of high signal intensity that we interpreted as scatter from the weld microstructure. The post-heat-treatment scan showed that the outlines were absent. The signal intensity along the joint line (within the yellow box) was slightly lower than elsewhere (and much lower than the same region of the pre-heat-treatment scan), a result of the slight difference in microstructure persisting at the joint line (see figure 39).

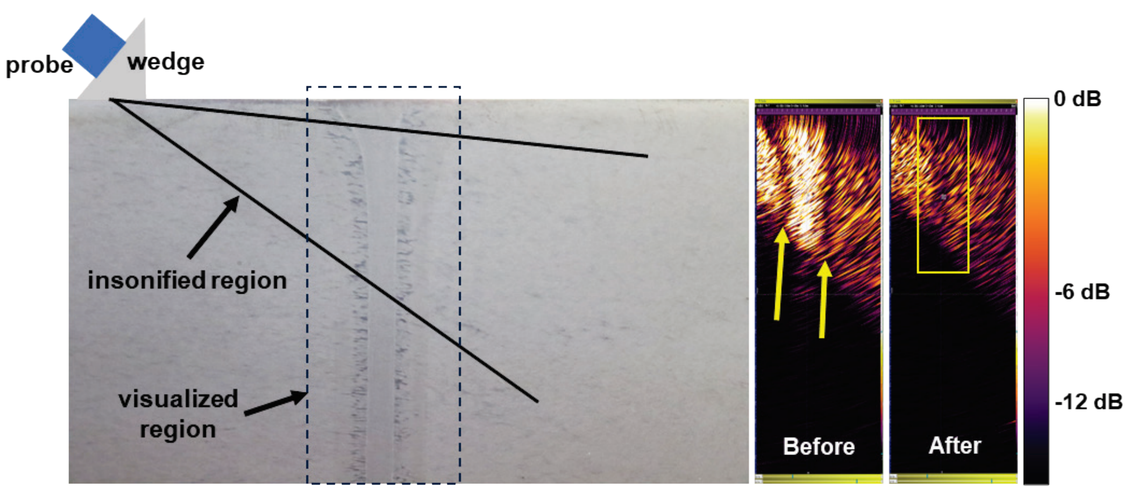


Figure 42: FMC results before and after heat treatment. The yellow arrows indicate shadows observed along the outline of the weld region. The yellow box indicates the joint line region.

After heat treatment, we noticed a small surface-breaking flaw on the bottom of the cut section at the joint line; see figure 43. The flaw was detectable using 0° UT from the end of the section (looking perpendicularly toward the weld) and appeared to be approximately 3 cm deep and 1.5 cm wide. The flaw was detected in the pre-heat-treatment A-scans and was possibly an unintentional LOF defect that occurred during beam pullout or shutdown at the end of the welding process. We note that the flaw was not visible in the 0° scan shown in figure 11. The flaw may have been missed due to its proximity to the edge of the block (recall that the 0° scans had about a 1 cm buffer from the edge of the blocks; see section 4.1).

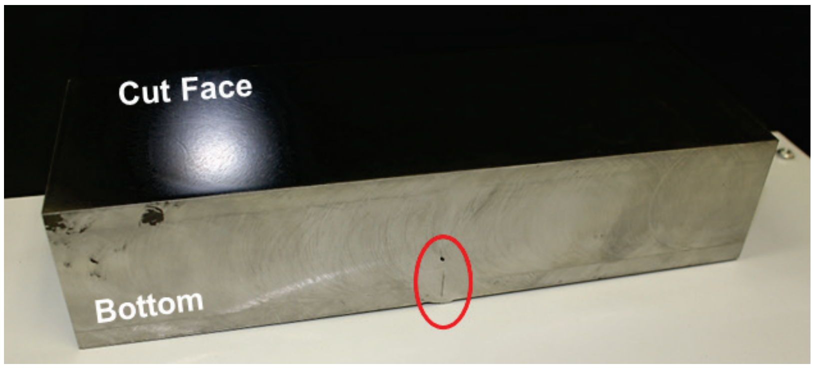


Figure 43: A flaw was noticed after heat treatment on the bottom surface of the section.

In summary:

- Visual observation showed that the heat treatment changed the weld microstructure in a manner that was expected (Gandy and Stover, 2018). The HAZ and melt zone were readily discernible prior to heat treatment while the weld joint line was faintly visible after heat treatment. Some subtle indications of post-heat-treatment microstructural differences along the joint line were visible under close inspection.

- 0° UT showed differences in attenuation and peak heights between the A-scan signatures on the weld and away from the weld prior to heat treatment, but these differences were less pronounced after heat treatment. After heat treatment, the measured attenuation of signals acquired adjacent to the weld decreased and the A-scan acquired on the joint line resembled the other A-scans.

- The FMC UT signature was qualitatively different after heat treatment. The shadows outlining the weld region were absent and there was less scatter signal.

Overall, the observations of the microstructure and UT signatures suggest that the heat treatment caused homogenization of the material microstructure such that the post-heat-treatment weld material appears visually and behaves ultrasonically similar to the parent material.

# 7.0 Summary

Results showed that pitch-catch scans using the TOFD setup were effective at both locating and depth-sizing all the flaws in simple butt-welds of EBW blocks. Pulse-echo UT techniques, such as those used on standard V welds, did not work well to locate and size the defects. With the simple butt-weld geometry, pulse-echo signals are either transmitted through the weld away from the probe or reflected by the unfused joint line away from the probe. In either case, no signals are received except for corner-trap echoes, which provide no depth information.

We point out that this was a limited study, examining the inspectability of one type of material with one type of electron beam weld with planar defects along the joint line. The carbon steel base material that the blocks were made from represents the best-case scenario for inspectability, meaning that the material properties had minimal adverse impacts on sound propagation. Therefore, by removing the material impacts as a variable, results confirm that welding defects in EBW joints can be detected and sized with appropriate NDE methods. If base materials are used that have microstructures that induce sound field scatter and attenuation, such as cast austenitic stainless steel, then adaptations to the NDE techniques will be needed. Such adaptations may include lower frequencies or longitudinal versus shear wave modes that better penetrate coarse-grained microstructures. Furthermore, the EBW blocks used herein did not have any filler material added during welding. In cases where a filler material is used, it may have an impact on inspectability, which should be adapted for as well.

The workshop on NDE of AMT highlighted several areas where research is needed. The work described in this report addressed several of these areas for EBW. Flaw detection was the most discussed workshop topic. We explored several types of EBW fabrication defects and showed that they are readily detectable when the correct UT method is used. The effects of material properties, such as grain microstructure, on inspectability was also emphasized in the workshop. We found that the microstructural characteristics of EBWs in carbon steel did not have any adverse impact on defect detection. Finally, NDE methods should be validated. We did not perform any destructive testing on the EBW blocks to determine the defect true-states or to validate the UT results, but it would be ideal to do so.

There were several specific findings in this report:

- The TOFD approach was the superior UT method for both detection and sizing. As shown in section 6.2.2, all the defects, including the LOP in block 4, were readily visible. Length and depth information could be obtained from all the defects. A downside of TOFD is that it requires access to both sides of the weld. When circumstances allow, we suggest using the TOFD approach for examining simple EBW butt-weld joints described in this report. We note that the UT signals observed using our TOFD setup are different from those typically observed with conventional TOFD (see figure 36), where tip diffracted signals are of primary interest. Our TOFD signals were also different from those from typical PE approaches, where defects result in strong echoes as opposed to weak signals. Therefore, we suggest that additional training will be needed to familiarize inspectors with how to recognize and interpret the types of signal responses that this TOFD method will give when inspecting EBW joints similar to those presented herein.

- FMC using PE showed corner echoes from unfused sections in blocks 2 and 3, the keyhole defect in block 2, and the fusion line in plate 3 (see figure 28 and 29, respectively). The LOP defect in plate 4 was faintly visible in the side view in figure 31.

Otherwise, defect depth information was not readily seen. Indeed, we observed that the signals from a fused region and an unfused region looked the same. The FMC images in section 6.2.1 also showed some weak signals from the weld region, likely due to scatter from the altered microstructure. As illustrated in figure 4, the smooth, vertical, planar joint line geometry of these blocks differs from the fusion lines seen in most conventional V welds, where the fusion planes are angled. Thus, the EBW joint line geometry poses particular challenges to standard PE inspection techniques, including FMC, because the echoes are reflected away from the probe.

- As described in section 6.2.3, the tandem approach detected strong corner echoes in blocks 2 and 3 along the unfused lengths; however, it did not provide any information about the depth of the LOF defects. Signals indicative of weld root were observed in the blocks, but there was no indication of the LOP defect in block 4. We speculate that a dynamic tandem approach would provide better results, but the complexity of executing such a method is not likely worth the trouble when unrestricted access from both sides of the weld is available. For cases with restricted (one-sided) access, the dynamic tandem approach may be the best option. Ultrasonic modeling and simulation should play a key role in developing the dynamic tandem approach by helping assure that appropriate probes and probe spacings are used. The probe size will determine the minimum probe spacing, which will impact sensitivity to shallow defects.

- We did not find radiography to be helpful in identifying the nature of the defects beyond what was apparent from visual observation. The thickness of the blocks was a limiting factor; the x-ray settings required to penetrate the blocks resulted in significant backscatter that compromised image quality (see section 6.1). The tight opening dimension and planar geometry of the defects was another limiting factor, as they did not provide enough contrast in the images. Even if defects could be identified with radiography, it is unlikely that any depth information could be obtained.

- Heat treatment performed on a section of block 1 improved ultrasonic transmission through the weld material. As shown in figure 40, when the weld region comprised the full metal path, the UT signals were less attenuated after heat treatment. However, the weld was not a factor in inspectability because the weld and HAZ represented a small fraction of the overall metal path during the TOFD scans. Although heat treatment is not necessary for the sole purpose of improving inspectability, it will not adversely affect inspectability if done for metallurgical reasons. Heat treatments are also not expected to repair defects or negatively impact the detectability of the types of welding defects discussed in this report.

# 8.0 References

ASME. 2023. *Full Matrix Capture Training Manual*. New York, NY: The American Society of Mechanical Engineers.

Cottrell, C. 1985. "Electron beam welding—a critical review." *Materials & design* 6 (6): 285-291.

Cumblidge, S. E., A. D. Cinson, and M. T. Anderson. 2010. *Evaluation of Ultrasonic Time-of-Flight Diffraction Data for Selected Control Rod Drive Nozzles from Davis Besse Nuclear Power Plant.* Pacific Northwest National Laboratory PNNL-19362.

EPRI. 2016. *Advanced Technology for Large-Scale (ATLAS) Powder Metallurgy–Hot Isostatic Pressing.*

EPRI. 2023a. *Deployment of Heavy Section Electron Beam Welding (EBW) Technologies.*

EPRI. 2023b. *Program on Technology Innovation: Design of Capsules for Powder Metallurgy Hot Isostatic Pressing via Computational Modeling.*

Faraone, K. M., R. G. Miller, and Z. Feng. 2022. *Review of Advanced Manufacturing Techniques and Qualification Processes for Light Water Reactors – Electron Beam Welding.* Oak Ridge National Laboratory.

Gandy, D., and C. Stover. 2018. "Advanced Manufacturing to Enable the Next Generation of Nuclear Plants." Advanced Manufacturing for Nuclear: Applications, Techniques, Needs, and Challenges and AMM Annual Program Review.

Gandy, D. W. 2015. "PM-HIP research for structural and pressuring retaining applications within the electric power industry." Structural Materials for Innovative Nuclear Systems, Idaho Falls, ID, USA.

Gandy, D. W. 2020. *PM-HIP and Electron Beam Welding Developments for Nuclear Applications.* Electrical Power Research Institute.

Gandy, D. W. 2021. "Development of a 316L SS Code Case Using Powder Metallurgy-Hot Isostatic Pressing." GAIN-EPRI-NEI AMM Qualification Workshop.

Hoelzer, D. T. 2022. *The Use of Powder Metallurgy and Hot Isostatic Pressing for Fabricating Components of Nuclear Power Plants.* Oak Ridge National Laboratory.

Jacob, R. E., S. L. Crawford, T. L. Moran, M. R. Larche, M. S. Prowant, A. A. Diaz, and C. A. Nove. 2019. *NDE Reliability Issues for the Examination of CASS Components.* Pacific Northwest National Laboratory.

Jacob, R. E., R. Montgomery, J. M. Harrison, M. Komarasamy, H. Jiang, and K. A. Ross. 2020. *Survey of Pre-service and In-service Nondestructive Evaluation Techniques of AMT-fabricated Components.* Pacific Northwest National Laboratory.

Kim, J., W. J. Lee, and H. W. Park. 2016. "The State of the Art in the Electron Beam Manufacturing Processes." *International Journal of Precision Engineering and Manufacturing* 17 (11): 1575-1585. https://doi.org/10.1007/s12541-016-0184-8.

Mandal, P., H. Lalvani, A. Barrow, and J. Adams. 2020. “Microstructural evolution of SA508 grade 3 steel during hot deformation.” *Journal of Materials Engineering and Performance* 29: 1015-1033.

Melfi, T. 2023. *DED-Wire (aka Welding) Use Case Update.* Lincoln Electric.

Nicolson, E., E. Mohseni, D. Lines, K. M. Tant, G. Pierce, and C. N. MacLeod. 2024. “Towards an in-process ultrasonic phased array inspection method for narrow-gap welds.” *NDT & E International*: 103074.

Prowant, M. S., C. Hutchinson, R. E. Jacob, J. Gillespie, A. E. Holmes, M. Hughes, and A. A. Diaz. 2023. *Evaluation of Advanced Phased-Array Techniques: Interim Results.* Pacific Northwest National Laboratory.

Tao, J., J. Wu, Z. Liu, J. Ma, Z. Liu, and W. Peng. 2022. “Influence of different beam oscillation patterns in electron beam welding of niobium sheets with different thickness.” *Materials* 15 (11): 3778.

# Appendix A – Presentation Abstracts

| Author and Affiliation | Presentation Title, ML Number, and Abstract |
|---|---|
| **David Rudland**<br>**John Wise**<br>NRC | **NRC Perspective on NDE of AMT**<br>ML23122A137 |
| **William Chuirazzi**<br>Idaho National Laboratory<br>**Robert Montgomery**<br>Pacific Northwest National Laboratory<br>**Amir Ziabari**<br>Oak Ridge National Laboratory | **DOE AMMT Efforts on Non-Destructive Evaluation for Additively Manufactured Nuclear Components**<br>ML23122A130<br><br>This talk focuses on non-destructive evaluation (NDE) efforts for additively manufactured (AM) nuclear components under the DOE office of Nuclear Energy Advanced Materials and Manufacturing Technologies (AMMT) program. The talk will cover 1) recent developments of AI-based X-ray CT reconstruction algorithms which allow for rapid and high-quality characterization of hundreds of parts, 2) investigations of correlations between neutron and X-ray CT imaging of AM components, and 3) investigations of ultrasonic techniques to characterize bulk material properties and as a means for inspection when component access is limited. We discuss the distinct capabilities of these techniques and highlight the synergies between them. Our plan is to leverage these techniques to qualify and certify AM components. |
| **Joseph Turner**<br>University of Nebraska-Lincoln | **Ultrasonic NDE for Metal Additive Manufacturing: Impact of Microstructure**<br>ML23122A139<br><br>Ultrasonic nondestructive evaluation is important for inspection of metal samples created by additive manufacturing (AM). Currently, challenges remain with respect to the uniformity of microstructures in metal AM parts. In this presentation, these microstructures and their impact on defect detection will be discussed using several examples. Prospects for future research will then be presented. |
| **Christopher Kube**<br>Pennsylvania State University | **In-process and Post-build NDE of Powder Bed Fusion Gr-91 Stainless Steel**<br>ML23122A132<br><br>An EOS M280 powder bed fusion system was integrated with several ultrasound sensors to monitor multiple parts simultaneously. The goal of the study was to use NDE during the process to discern slight difference in part microstructure. The in process measurements will be highlighted in addition to post-build resonant ultrasound spectroscopy. Discussion of all of the results, lessons learned, and outlook to be given. |

| | |
|---|---|
| **Jesse Waller**<br>New Mexico State University | **NDE Inspection Needs for Additively Manufactured Components: A Technology and Standardization Gap Analysis**<br>ML23122A128<br><br>Version 3.0 of the ANSI/America Makes Standardization Roadmap for Additive Manufacturing is currently in public review. Key gaps related to the nondestructive evaluation (NDE) and qualification and certification approaches used by the aerospace industry are discussed. Common challenges faced by the aerospace industry and fracture critical spaceflight hardware and the nuclear industry and safety critical hardware are addressed. For example, a new NDE gap in the Roadmap has been introduced that encompasses in-service inspection of safety-critical components meeting the quality and performance requirements of the nuclear industry and regulatory authorities throughout the components' lifetime. |
| **David G. Moore**<br>**Ciji L. Nerson**<br>**Caleb A. Schauble**<br>**Matthew J. Dennis**<br>Sandia National Laboratories | **Characterization of Additively Manufactured Samples with Mechanical Testing and Nondestructive Inspection Techniques: A Path Forward for Qualification**<br>ML23122A140<br><br>Additively manufactured (AM) components contain discontinuities, indications, and defects which can change the component's mechanical performance during qualification or while the part is in-service. The inspection uncertainty and misidentification of discontinuities created during the AM build limits the use of this manufacturing process for aerospace applications. Current research at Sandia National Laboratories is addressing these concerns by focusing on mechanical characteristics, metallurgical techniques, and nondestructive inspection methods to assess uniaxial tensile specimens, which in turn will optimize the AM machine set-up parameters. This presentation focuses on a direct metal laser sintering (DMLS) powder bed fusion machine that is being prepared for production use. A background on Sandia National Laboratories' research efforts and how nondestructive evaluation assists design teams will be described. Four case studies will be summarized. Computed tomography, eddy current, and ultrasonic test methods will inspect AM specimens, and the advantages and disadvantages of each inspection method will be presented. The use of material strength testing, microstructural analysis, and nondestructive inspection techniques will be described, along with a roadmap for identifying limits for the qualification of AM materials. |

| | |
|---|---|
| **Alexander Heifetz**<br>Argonne National Laboratory | **Detection of Microscopic Subsurface Defects in Metals with Unsupervised Learning of Pulsed Infrared Thermography Images**<br>(no ML number)<br><br>Pulsed infrared thermography (PIT) is a nondestructive method for imaging of internal defects in solids using heat transfer. Advantages of PIT include non-contact and one-sided material examination using compact instrumentation. PIT involves deposition of heat pulse on material surface with a flash lamp. As heat is diffusing from the surface into material bulk, material surface temperature is monitored with fast-frame Infrared (IR) camera via measuring blackbody radiation. Presence of internal defects is detected via appearance of transient temperature “hot spots” on material surface due to local thermal resistance of defects. Limitations of imaging resolution with PIT include blurring due to heat diffusion, detection sensitivity of IR camera, and uneven heating of the specimen. We investigated experimental limits of PIT detection of subsurface defects in high strength corrosion resistant stainless steel 316 alloy. Metallic specimens with calibrated microscopic flat bottom hole defects, with diameters in the range from 200μm to 75μm, were produced using electro discharge machining (EDM) drilling. PIT images were processed with the unsupervised learning (UL) based spatial-temporal blind source separation (STBSS) algorithm to enhance visibility of defects. While the raw PIT data did not show any material defects, using STBSS algorithm to process PIT reveals defects as small as 100μm in diameter. To the best of our knowledge, this is the smallest reported size of defect in a metal imaged with PIT. |
| **Pingsha Dong**<br>University of Michigan | **Effects of Distributed Defects and Interactions on Fatigue Behavior of AM Components and a Zone-based NDE Methodology**<br>ML23122A129<br><br>Recent investigations have shown that fatigue behavior of metal AM components exhibits a significant difference from that typically seen in wrought materials. This can be attributed mainly to the presence of distributed geometric discontinuities and their interactions, particularly at stress riser locations. In this talk, some of the recent important findings are presented on effects of distributed defects and their interactions on fatigue behaviors of AM parts, particularly on test specimens containing stress raisers. The results suggests that a zone-based NDE inspection procedure should be a key enabler for ensuring both fitness-for- service of AM components and cost-effective deployment of AM technologies in safety-critical applications. |

| | |
|---|---|
| **Steve Mahaut**<br>CEA-LIST | **NDE and Monitoring for AM Parts and Process**<br>ML23122A136<br><br>In this talk, several studies carried out at CEA will be presented, related to industrial and collaborative projects including various AM processes: powder bed fusion, wire arc additive manufacturing, direct energy deposition. Both NDE on built parts and online monitoring tools have been investigated, aiming at ensuring the quality of AM parts. Different NDE techniques (RT and CT, UT, ET) as well as specific NDE data analysis and correlation (with AM settings and building parameters) will be discussed. |
| **Udisien Woy**<br>Nuclear Advanced Manufacturing Research Centre | **A Systemic Perspective on Developing Non-destructive Evaluation (NDE) Strategies for Additive Manufacturing (AM) Applications in Nuclear**<br>ML23122A126<br><br>Non-destructive evaluation (NDE) is an involving and encompassing endeavor that supports important decisions concerning the appropriateness of critical industrial structures, including those fabricated via additive manufacturing (AM). However, the potential advantages of these advanced manufacturing technologies, such as the ability to simplify the fabrication of complex geometries, are presently constrained by limited understanding of the resulting risk profile. Correspondingly, systemic factors influencing discreet AM technologies and procedures are explored, to accentuate the efficacy of different NDE methods for accurately and reliably informing validation requirements. |
| **Ron Aman**<br>EWI | **Considerations and Experience Applying NDE to AM Materials and Components**<br>ML23167A053<br><br>EWI has been developing and applying NDE techniques to additive manufacturing materials for nearly 20 years. Special considerations need to be observed with AM materials due to complex geometry produced and unique microstructures observed in these materials. The application of NDE methodologies to large-scale Directed Energy Deposition (DED) aero structures, standard qualification builds and a new approach to use zone criticality and process observations to inform NDE processing will be discussed. |

| | |
|---|---|
| **George Connolly,** EPRI, Inc.<br>**John Shingledecker,** EPRI, Inc.<br>**Anand Kulkarni,** Siemens Corp.<br>**Jeff Crandall,** CCAT, Inc.<br>**Bruce Greer**, EPRI, Inc.<br>**Stephen Tate,** EPRI, Inc. | **UT and FMC/TFM for Additively-Manufactured Components: Recent Experiences**<br>ML23122A133<br><br>We present a summary of recent UT scanning results, from both conventional UT and Full Matrix Capture/Total Focusing Method (FMC/TFM), and observations therefrom upon a series of AM coupons and reference standards. The components, designed in-house at EPRI, are printed using laser-based powder bed fusion (LPBF). The UT results are correlated against RT results and visual microstructural characterization. A procedure to quantify UT sensitivity to various reflectors is presented. We also comment upon UT performance in application to AM coupons composed of more than one metal. |
| **Andrew Gavens** Naval Nuclear Laboratory<br>**Benjamin Palmer** Naval Nuclear Laboratory<br>**James Eliou** Naval Nuclear Laboratory<br>**Eric Biedermann** Vibrant Corporation<br>**Garret Gatewood** Vibrant Corporation | **Using Process Compensated Resonance Testing to Differentiate Laser Powder Bed Fusion Additively Manufactured Witness Coupons Produced with Varying Process Parameters**<br>ML23122A135<br><br>Production of high quality additively manufactured (AM) components requires a consistent manufacturing process. Variability between builds, AM equipment manufacturers, and AM facilities using laser powder bed fusion (L-PBF) systems is currently a concern. Production of small witness coupons placed throughout a build volume provides material for evaluation upon completion of a build. 316L stainless steel witness coupons were built using a variety of L-PBF build conditions. These coupons were then evaluated with process compensated resonance testing (PCRT). PCRT is a fast, quantitative nondestructive evaluation and process control method that analyzes the resonance frequencies of a component. It was demonstrated that PCRT could differentiate coupons manufactured with default conditions from those produced with ±5% or greater variation in laser power or velocity. Using PCRT to nondestructively evaluate witness coupons produced alongside a component confirms that the equipment is operating correctly and can manufacture high quality material. This increases confidence that the AM build was performed under the desired process conditions and supports the overall component qualification. |

| | |
|---|---|
| **Adam Wick**<br>**James Eliou**<br>**Nicholas Cosentino**<br>**Andrew Turnbull**<br>Naval Nuclear Laboratory | **Embedding Surface-connected Cracks in 316L Stainless Steel Laser Powder Bed Fusion Manufactured Pipe Specimens for Qualification of Phased Array Ultrasonic Testing Inspection Techniques**<br>ML23122A134<br><br>This talk presents details and best practices for designing and fabricating cracked pipe specimens for qualification of phased array ultrasonic testing (PAUT) techniques using metal additive manufacturing. Conventionally, specimens like this are made by implanting electro-discharge machined (EDM) notches in pre-built pipes or by contract with a flawed specimen vendor that will implant more realistic cracks using proprietary processes. Fabricating PAUT qualification specimens using additive manufacturing allows for more realistic cracks (including realistic inter-granular stress corrosion cracking) placed and sized more accurately at a lower cost and a shorter turnaround time. Computed tomography has been used to image existing cracks to inform design of new ones and to verify proper placement and size of additively manufactured cracks. |
| **Peter Collins**<br>Iowa State University | **On the Process-Structure-Property-Performance for Additively Manufactured Titanium Alloys**<br>ML23122A138<br><br>An Integrated Computational Materials Engineering (ICME) framework has been developed and applied for multiple variants of large-area additive manufacturing of the aerospace alloy Ti-6Al-4V. The approach permits the integration of (i) mesoscopic models of heat-transfer and a moving energy source with (ii) kinetic and thermodynamic models for the prediction of key aspects of the materials state and the subsequent (iii) uniaxial tensile properties and (iv) statistical methods of developing so-called “design allowable curves”. This previous effort has demonstrated which aspects of the materials state seem to matter for this particular alloy, as well as correlated features that could be measured. This work indicates the need to develop methods to measure materials state and materials composition, both of which can be controlled through the process. The control of the state, including NDE impact, will be presented. Of particular interest is the need to measure texture, defects, and composition. Insights into emergent work, as well as what is likely to be possible, will be presented. |

| | |
|---|---|
| **Reza Zoughi**<br>**Peter Collins**<br>Center for Nondestructive Evaluation, Iowa State University | **A Vision for Comprehensively Bringing Additive Manufacturing (AM) and Nondestructive Evaluation (NDE) Together in a National Testbed**<br>ML23122A127<br><br>We aim to establish a *unique* and *comprehensive national testbed facility* where engineers and scientist can collaborate to achieve one primary objective: Enable Next-Generation Additive Manufacturing (AM), where *in-process* and *post-manufacture* Nondestructive Evaluation (NDE) techniques are integrally implemented. The collaborating scientists and engineers will achieve this by adopting a holistic view of AM, and intentionally integrating individual research and development (R&D) activities into a larger framework which simultaneously considers: the AM processes; the materials involved; the build quality; the geometry/topology; and the desired properties and performance as defined by an end-user. These aspects are understood to be both hierarchical and potentially hybrid in nature (e.g., multiple AM processes for a given part, multiple materials, hierarchical topologies, etc.). *Quality assurance* underpins all of these efforts. Thus, this proposed Facility uniquely emphasizes the importance of integrating nondestructive evaluation (NDE) techniques directly into the AM paradigm and the emergent economy. Our collaborating scientists and engineers will conduct their activities while optimizing existing nondestructive evaluation (NDE) techniques and developing new and innovative methods for the sole purposes of *in-process* and *post-manufacture* inspection of the AM processes and products. This presentation outlines these objectives and discuss a roadmap for achieving them. |